Research Square

Preprints are preliminary reports that have not undergone peer review.
They should not be considered conclusive, used to inform clinical practice,
or referenced by the media as validated information.

A fictitious-source formulation for direct numerical simulation of turbulent boundary layers in prescribed pressure gradients

Alessandro Ceci

alessandro.ceci@gssi.it

Gran Sasso Science Institute

Christoph Wenzel

University of Stuttgart

Sergio Pirozzoli

Sapienza University of Rome

Research Article

Keywords: Direct numerical simulation, pressure-gradient boundary layers, compressible turbulence, fictitious source terms, quasi-one-dimensional Euler equations

Posted Date: October 30th, 2026

DOI: https://doi.org/10.21203/rs.3.rs-11223057/v1

License: This work is licensed under a Creative Commons Attribution 4.0 International License.
Read Full License

Additional Declarations: No competing interests reported.

A fictitious-source formulation for direct numerical simulation of turbulent boundary layers in prescribed pressure gradients

Alessandro Ceci · Christoph Wenzel · Sergio Pirozzoli

Abstract A fictitious-source formulation is introduced for prescribing general streamwise pressure-gradient distributions at the boundary-layer edge in compressible boundary-layer simulations while retaining a flat Cartesian domain. The method constructs a thermodynamically consistent quasi-one-dimensional isentropic outer-flow target, from which compatible mass, streamwise-momentum and total-energy source terms are derived. These replace the streamtube expansion or contraction associated with the target evolution and are blended out towards the boundary layer, leaving its internal dynamics unforced. The formulation is validated for low-speed adverse- and favourable-pressure-gradient turbulent boundary layers against expanding- and contracting-domain reference simulations sharing the same flat lower wall. The prescribed edge-velocity development, wall friction, mean velocity profiles and turbulent stresses are reproduced with close quantitative agreement. At Mach 2, forced flat-wall configurations are compared with curved-wall boundary layers at closely matched edge-velocity distributions. The prescribed edge velocity and pressure are recovered with only small deviations, whereas the different wall and streamline geometries produce measurable differences in boundary-layer development despite the closely matched outer-flow histories. A momentum-integral analysis including streamline-curvature terms further underlines the coupled nature of the curvature influence, which affects several contributions through the modified boundary-layer development rather than appearing as a single explicit curvature term. The method thereby enables pressure-gradient distributions to be prescribed independently of wall geometry, particularly in compressible and supersonic boundary layers.

Keywords Direct numerical simulation · pressure-gradient boundary layers · compressible turbulence · fictitious source terms · quasi-one-dimensional Euler equations

1 Introduction

Compressible turbulent boundary layers subject to streamwise pressure gradients occur in many high-speed aerodynamic configurations, including external lifting surfaces, compression systems, inlets and turbomachinery passages. Their dynamics is considerably richer than that of the canonical zero-pressure-gradient (ZPG) boundary layer because the mean development depends on the complete pressure-gradient history and on its interaction with compressibility, wall thermal conditions and, in practical geometries, wall curvature. Even in incompressible flow, pressure-gradient turbulent boundary

Alessandro Ceci (corresponding author)
Gran Sasso Science Institute, Viale Francesco Crispi 7, 67100 L'Aquila, Italy
E-mail: alessandro.ceci@gssi.it

Christoph Wenzel
Institute of Aerodynamics and Gas Dynamics (IAG), University of Stuttgart, Wankelstraße 3, 70563 Stuttgart, Germany

Sergio Pirozzoli
Dipartimento di Ingegneria Meccanica e Aerospaziale, Sapienza Università di Roma, Via Eudossiana 18, 00184 Roma, Italy

layers are sensitive to history effects [13, 20]. In compressible flow, the interpretation is further complicated by the coupling between streamwise acceleration or deceleration, density variation and Mach number effects [17, 24].

The numerical realization of boundary layers, both laminar and turbulent, subject to a prescribed pressure gradient is, however, not straightforward. In a conventional numerical setup, the pressure distribution can generally only be prescribed at the upper domain boundary, several boundary-layer thicknesses away from the wall. Owing to the wall-normal variation of the outer potential flow, the pressure imposed there may differ substantially from that established at the boundary-layer edge, and this evolution therefore has to be anticipated when defining the boundary condition. The problem is particularly pronounced in supersonic flow, where pressure disturbances propagate along inclined waves, whereas in subsonic flow approximately wall-normal isobars may often provide at least a reasonable approximation. Precise control of the pressure distribution at the boundary-layer edge is nevertheless important for many applications, for instance when pressure- gradient and wall-curvature effects are to be studied independently or when experimentally measured pressure distributions are to be reproduced in high-fidelity simulations. A simple streamwise momentum forcing, as commonly used in channel flows, may generate a pressure gradient, but does not enforce a thermodynamically compatible evolution of density, temperature and mass flux. Control of the complete boundary-layer-edge state therefore remains indirect.

Several strategies have been used to generate pressure gradients in DNS and high-fidelity simulations. Subsonic boundary layers can be driven by prescribing an appropriately adjusted outer pressure or velocity distribution, by modifying the upper boundary, by analytically integrating a potential-flow solution, or by using predictor–corrector procedures that match a target wall pressure [2, 7, 11, 23]. In supersonic flow, pressure gradients are often produced by compression ramps, expansion corners, reflected waves, or curved surfaces [1, 8, 18, 22, 26]. These approaches are physically meaningful, but they may introduce shock-wave/boundary-layer interaction, separation, streamline curvature, or Görtler-type effects that are not part of the pressure-gradient mechanism itself [4, 6, 12, 19, 21, 27], or may not allow sufficiently accurate control of arbitrary target pressure-gradient distributions [24]. This makes it difficult to isolate the response to a specified pressure-gradient distribution from that associated with its geometrical realization.

1.1 Goals of the study

This paper addresses the computational problem of imposing a prescribed pressure-gradient distribution in simulations while retaining a flat wall and a Cartesian mesh. The method adds fictitious source terms to the compressible Navier–Stokes equations. The source terms are constructed from a thermodynamically consistent quasi-one-dimensional target outer flow following a prescribed external velocity or pressure distribution. The distinctive feature of the formulation is that the complete isentropic edge-state evolution is prescribed through mutually compatible mass, momentum and energy source terms, rather than through streamwise momentum forcing alone. They replace the streamtube expansion or contraction that would naturally accompany this inviscid evolution by corresponding volumetric mass, streamwise-momentum and energy sources. The resulting source terms are equivalent, at the one-dimensional level, to the effect of an inviscid variable-area flow. In the DNS conducted for verification, the sources are applied in the outer flow and blended out towards the boundary layer, thereby generating the prescribed outer-flow evolution without directly forcing the boundary layer itself. The multidimensional boundary-layer response, including the associated wall-normal motion, remains part of the Navier–Stokes solution.

1.2 Study design

To validate the method and demonstrate its utility, both subsonic and supersonic pressure-gradient boundary layers are considered. The low-speed cases provide the basic validation of the forcing strategy by comparing geometrical reference cases in expanding and contracting domains with forced flat-plate

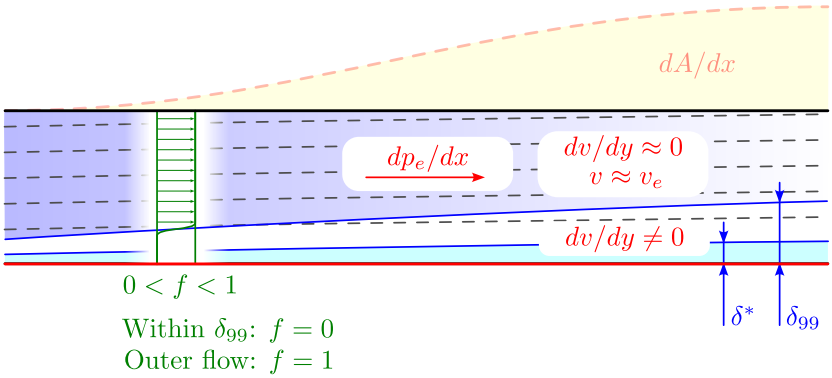


Fig. 1 Schematic comparison of the equivalent variable-area quasi-one-dimensional outer-flow interpretation and its embedding into the flat Cartesian boundary-layer DNS. In the Cartesian formulation, the source terms replace the streamtube expansion or contraction associated with the prescribed target evolution and are blended to zero inside the boundary layer. The wall-normal motion generated by the developing boundary layer remains part of the multidimensional Navier–Stokes solution

simulations, later referred to as configurations B and C, respectively. Since both realizations retain the same flat lower wall, this comparison directly assesses the replacement of the geometrically induced outer-flow deflection by the fictitious source terms.

The same formulation is then applied to Mach-2 boundary layers. Curved-wall DNS and forced flat-plate simulations, later referred to as configurations A and C, respectively, are constructed with closely matched boundary-layer-edge velocity distributions. This provides a controlled means of examining pressure-gradient boundary layers with and without the wall- and streamline-curvature effects associated with the geometrical realization.

The remainder of the paper is organized as follows. The fictitious-source formulation is introduced in §2, followed by the numerical method and computational configurations in §3. The low-speed validation is presented in §4, and the supersonic application and comparison with curved-wall DNS in §5. The main findings are summarized in §6.

2 Fictitious-source formulation

The purpose of the forcing is to reproduce, in a flat Cartesian DNS domain, a prescribed outer pressure or velocity evolution. To this end, we first define a thermodynamically consistent quasi-one-dimensional inviscid target state and derive source terms such that this state satisfies the corresponding forced one-dimensional conservation equations, see Fig. 1. The sources replace the streamtube expansion or contraction that would naturally accompany the target evolution. The same source vector follows from the quasi-one-dimensional Euler equations for inviscid variable-area flow, which therefore provide a useful physical interpretation. Finally, the sources are embedded into the multidimensional Navier–Stokes equations and applied in the outer flow while being blended out towards the boundary layer.

2.1 Prescribed quasi-one-dimensional target state

To construct the desired target outer-flow state, we consider a steady quasi-one-dimensional inviscid flow with prescribed edge velocity $u_e(x)$ or pressure $p_e(x)$. The target flow is assumed isentropic. Hence,

$$H_e = h_e + \frac{u_e^2}{2} = H_t = \text{const.}, \tag{1}$$

while the streamwise momentum balance gives

$$\frac{\mathrm{d}p_e}{\mathrm{d}x} = -\rho_e u_e \frac{\mathrm{d}u_e}{\mathrm{d}x}. \tag{2}$$

Given either $u_e(x)$ or $p_e(x)$ and one reference thermodynamic state, the complete target state follows from constant total enthalpy and the standard isentropic relations on the selected Mach-number branch. The prescribed distribution must therefore correspond to a smooth isentropic evolution on the selected subsonic or supersonic branch; shock-containing or entropy-generating target states are outside the scope of the present formulation. The isentropic assumption applies only to the prescribed inviscid outer-flow target and does not constrain the thermal boundary condition at the wall; heated or cooled walls can therefore be treated without modification of the forcing formulation.

To determine the required forcing, we consider the quasi-one-dimensional conservation equations with source terms,

$$\frac{\partial \rho}{\partial t} + \frac{\partial (\rho u)}{\partial x} = S_\rho, \tag{3}$$

$$\frac{\partial (\rho u)}{\partial t} + \frac{\partial (\rho u^2 + p)}{\partial x} = S_{\rho u}, \tag{4}$$

$$\frac{\partial (\rho E)}{\partial t} + \frac{\partial (\rho u H)}{\partial x} = S_{\rho E}. \tag{5}$$

The source terms are chosen such that the prescribed target state (ρ_e, u_e, p_e, H_e) is an exact steady solution,

$$S_\rho = \frac{\mathrm{d}(\rho_e u_e)}{\mathrm{d}x}, \tag{6}$$

$$S_{\rho u} = \frac{\mathrm{d}(\rho_e u_e^2 + p_e)}{\mathrm{d}x}, \tag{7}$$

$$S_{\rho E} = \frac{\mathrm{d}(\rho_e u_e H_e)}{\mathrm{d}x}. \tag{8}$$

Using the isentropic relation $\mathrm{d}p_e = a_e^2 \mathrm{d}\rho_e$, with $a_e^2 = \gamma p_e/\rho_e$, together with (2), gives

$$\frac{1}{\rho_e}\frac{\mathrm{d}\rho_e}{\mathrm{d}x} = -M_e^2 \frac{1}{u_e}\frac{\mathrm{d}u_e}{\mathrm{d}x}, \tag{9}$$

and therefore

$$S_\rho = \frac{\mathrm{d}(\rho_e u_e)}{\mathrm{d}x} = \rho_e (1 - M_e^2)\frac{\mathrm{d}u_e}{\mathrm{d}x}. \tag{10}$$

For the momentum source,

$$S_{\rho u} = u_e \frac{\mathrm{d}(\rho_e u_e)}{\mathrm{d}x} + \rho_e u_e \frac{\mathrm{d}u_e}{\mathrm{d}x} + \frac{\mathrm{d}p_e}{\mathrm{d}x} = u_e S_\rho, \tag{11}$$

where (2) has been used. Since $H_e = H_t = \text{const.}$,

$$S_{\rho E} = H_e S_\rho. \tag{12}$$

Introducing

$$\chi(x) \equiv -\frac{S_\rho}{\rho_e u_e}, \tag{13}$$

gives

$$\chi = (M_e^2 - 1)\frac{1}{u_e}\frac{\mathrm{d}u_e}{\mathrm{d}x}, \tag{14}$$

or

$$\chi = -\frac{M_e^2 - 1}{\gamma M_e^2}\frac{1}{p_e}\frac{\mathrm{d}p_e}{\mathrm{d}x}. \tag{15}$$

The source terms can therefore be written as

$$S_\rho = -\rho_e u_e \chi, \tag{16}$$

$$S_{\rho u} = u_e S_\rho, \tag{17}$$

$$S_{\rho E} = H_e S_\rho. \tag{18}$$

Here, the mass source sets the required quasi-one-dimensional mass-flux evolution, while the momentum and energy sources ensure that the added or removed mass carries the target streamwise momentum and total enthalpy.

2.2 Equivalent variable-area interpretation

The source formulation also admits a simple geometrical interpretation. For a steady quasi-one-dimensional inviscid flow through a variable-area nozzle or diffuser, conservation of mass gives $\mathrm{d}(\rho u A)/\mathrm{d}x = 0$ and therefore

$$\frac{\mathrm{d}(\rho u)}{\mathrm{d}x} = -\rho u \frac{1}{A}\frac{\mathrm{d}A}{\mathrm{d}x}. \tag{19}$$

With

$$\chi = \frac{1}{A}\frac{\mathrm{d}A}{\mathrm{d}x} = \frac{\mathrm{d}\log A}{\mathrm{d}x}, \tag{20}$$

this gives

$$S_\rho = -\rho_e u_e \chi, \tag{21}$$

together with

$$S_{\rho u} = u_e S_\rho, \qquad S_{\rho E} = H_e S_\rho. \tag{22}$$

At the quasi-one-dimensional level, the source vector is therefore identical to that obtained by rewriting an inviscid variable-area flow as an equivalent constant-area problem with volumetric sources. In this sense, the source terms replace the streamtube expansion or contraction that would otherwise generate the prescribed inviscid outer-flow evolution.

2.3 Embedding into the multidimensional Navier–Stokes equations

For the DNS, the one-dimensional source vector is embedded into the compressible Navier–Stokes equations as

$$\frac{\partial \rho}{\partial t} + \frac{\partial(\rho u_j)}{\partial x_j} = S_\rho, \tag{23}$$

$$\frac{\partial(\rho u_i)}{\partial t} + \frac{\partial(\rho u_i u_j)}{\partial x_j} + \frac{\partial p}{\partial x_i} - \frac{\partial \sigma_{ij}}{\partial x_j} = S_{\rho u_i}, \tag{24}$$

$$\frac{\partial(\rho E)}{\partial t} + \frac{\partial(\rho u_j H)}{\partial x_j} - \frac{\partial q_j}{\partial x_j} = S_{\rho E}, \tag{25}$$

where only the streamwise momentum equation is forced, such that

$$S_{\rho u_i} = S_{\rho u}\delta_{i1}. \tag{26}$$

Here, σ_{ij} is the viscous stress tensor and q_j is the heat flux. The source terms are constructed from the prescribed quasi-one-dimensional target state and are therefore known functions of x.

The source vector is applied through a wall-normal blending,

$$\mathbf{S}(x, y, z, t) = f(x, y, z, t)\mathbf{S}_e(x), \tag{27}$$

where f is determined locally from the instantaneous flow field. It approaches unity in the weakly rotational outer flow and is smoothly reduced towards zero across the outer part of the rotational boundary-layer region. The forcing therefore follows the instantaneous boundary-layer development without requiring a prescribed or time-averaged boundary-layer edge. The particular local criterion used in the present simulations is described in § 4.1.

The boundary layer itself is consequently allowed to evolve without direct forcing and to generate the wall-normal motion associated with its growth. The quasi-one-dimensional construction is used only to define the source vector and does not otherwise constrain the multidimensional Navier–Stokes solution. This multidimensional response extends into the forced outer region, such that a finite wall-normal velocity is retained also outside the boundary layer. The forcing does not prescribe the wall-normal velocity or impose $\partial(\rho v)/\partial y = 0$; rather, these quantities follow from the multidimensional Navier–Stokes solution. Likewise, the pressure field adjusts to the resulting multidimensional flow, while its streamwise evolution is governed primarily by the imposed quasi-one-dimensional forcing. A more detailed discussion of the forcing mask and of the resulting wall-normal flow adjustment is given in § 4.1.

2.4 Construction for a prescribed pressure or velocity distribution

The procedure used in the DNS is as follows.

1. Choose the target outer pressure $p_e(x)$ or velocity $u_e(x)$ over the streamwise interval of interest. In the Mach-2 cases, $u_e(x)$ is represented analytically through power laws, avoiding numerical noise in its derivative.
2. Determine the corresponding thermodynamic target state. For prescribed $u_e(x)$, $T_e(x)$ follows from constant total enthalpy, (1), while p_e and ρ_e follow from the isentropic relations. For prescribed $p_e(x)$, the isentropic relations are inverted on the selected subsonic or supersonic branch to obtain $M_e(x)$ and the remaining target quantities.
3. Compute the source terms from the prescribed target state,

$$S_\rho = \rho_e(1 - M_e^2)\frac{\mathrm{d}u_e}{\mathrm{d}x}, \tag{28}$$

$$S_{\rho u} = u_e S_\rho, \tag{29}$$

$$S_{\rho E} = H_e S_\rho. \tag{30}$$

   For a prescribed pressure distribution, the equivalent expression in terms of $\mathrm{d}p_e/\mathrm{d}x$ may be used.
4. Apply the source vector to the discrete right-hand side of the conservative variables at each Runge–Kutta substep, using the blending defined in (27). No metric terms, grid Jacobians or curvilinear fluxes are introduced, and the method enters the solver as a local source-term contribution.

The zero-pressure-gradient limit is recovered for $\mathrm{d}u_e/\mathrm{d}x = 0$, for which all source terms vanish. In supersonic flow, an FPG corresponds to an increasing equivalent area and $S_\rho < 0$, whereas an APG corresponds to a contracting area and $S_\rho > 0$.

2.5 Low-speed limit and relation to body-force approaches

In the low-speed limit, the present formulation reduces to a form closely related to the pressure-gradient forcing commonly used in canonical simulations. For an incompressible quasi-one-dimensional target flow, $u_e A = \text{const.}$ together with the Bernoulli relation. Equations (23)–(25) then give

$$\frac{\partial u_j}{\partial x_j} = \frac{\mathrm{d}u_e}{\mathrm{d}x}, \tag{31}$$

$$\frac{\partial u_i}{\partial t} + \frac{\partial (u_i u_j)}{\partial x_j} + \frac{1}{\rho}\frac{\partial p}{\partial x_i} - \nu\frac{\partial^2 u_i}{\partial x_j \partial x_j} = -\frac{1}{\rho}\frac{\mathrm{d}p_e}{\mathrm{d}x}\delta_{i1}. \tag{32}$$

The streamwise momentum forcing is therefore accompanied by a compatible divergence source representing the streamtube expansion or contraction associated with the prescribed outer-flow evolution. If only the streamwise momentum equation is forced, a pressure gradient can likewise be generated, but the corresponding cross-stream adjustment is then left entirely to the multidimensional flow. In the present approach, the mass, momentum and energy sources are instead constructed jointly from the prescribed quasi-one-dimensional target state. This distinction becomes more important in compressible flow, where velocity, pressure, density and temperature vary simultaneously. The coupled source formulation therefore prescribes a mutually compatible quasi-one-dimensional evolution of mass, streamwise momentum and total energy, rather than merely supplying a streamwise momentum input.

3 Methodology and numerical setup

The numerical assessment is based on the three configurations summarized in Fig. 2. At subsonic speed, geometrical reference cases with a variable upper boundary (configuration B) are compared with forced flat-plate simulations (configuration C). At Mach 2, curved-wall DNS (configuration A) are compared with the forced flat-plate configuration C at matched boundary-layer-edge velocity distributions.

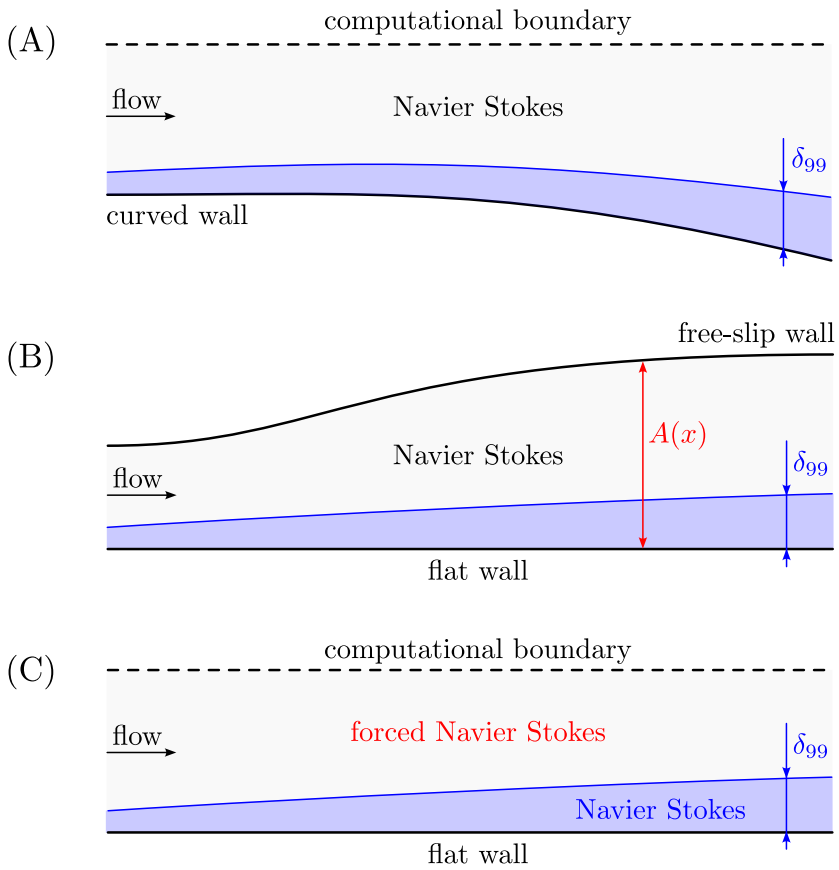


Fig. 2 Flow configurations considered in the present study. (A) Boundary layer over a curved lower wall. (B) Boundary layer with a flat lower wall and variable upper boundary. (C) Forced flat-plate configuration in which the prescribed outer-flow evolution is generated by the fictitious source terms (10)–(12)

3.1 Numerical method

All simulations employ the compressible DNS solver STREAmS [3, 16]. The working fluid is air, modelled as a calorically perfect gas with specific-heat ratio $\gamma = 1.4$. The viscous stresses are evaluated according to the Newtonian constitutive law. The dynamic viscosity is computed using Sutherland's law, with $T_{\mathrm{ref}} = 288.15\,\mathrm{K}$ and $S = 110.4\,\mathrm{K}$, whereas the thermal conductivity is obtained assuming a constant Prandtl number, $Pr = 0.72$. The convective fluxes are discretized using a sixth-order skew-symmetric central-difference scheme [14]. The diffusive fluxes, expanded in Laplacian form, are discretized using sixth-order central formulas, and time advancement is performed with a third-order Runge–Kutta scheme [25]. The fictitious source terms enter as local right-hand-side contributions and therefore require no modification of the conservative flux discretization. The instantaneous inflow velocity field is obtained by applying the inverse Van Driest transformation to an incompressible mean velocity profile and to velocity fluctuations generated through a recycling–rescaling procedure with spanwise shift [15]. Temperature fluctuations are reconstructed from the streamwise velocity fluctuations according to the strong Reynolds analogy [9]. The wall temperature is prescribed as the local recovery temperature, $T_w = T_r$, where

$$T_r = T_e \left(1 + r\,\frac{\gamma - 1}{2} M_e^2\right), \tag{33}$$

with $r = Pr^{1/3}$. The wall temperature is constant in time at each streamwise location but varies with the prescribed local edge state. Periodicity is imposed in the spanwise direction. The remaining boundary conditions depend on the flow regime and are specified below.

Table 1 DNS cases used for validation. The prefix "i" denotes the subsonic low-speed cases and "c" the Mach-2 cases. APG and FPG denote adverse and favourable pressure gradients, respectively. The suffixes F, N and C denote forced flat-plate, nozzle-reference and curved-wall configurations, respectively. All simulations use $\Theta = 1$.

Case	Configuration	PG distribution	Nominal β_K range	Line-style
iAPG-N	expanding nozzle	natural	$0 \rightarrow 1.5$	
iAPG-F	forced flat plate	matched to iAPG-N	$0 \rightarrow 1.5$	
iFPG-N	converging nozzle	natural	$0 \rightarrow -0.7$	
iFPG-F	forced flat plate	matched to iFPG-N	$0 \rightarrow -0.7$	
cZPG	flat plate	-	0	
cAPG-C	curved wall	natural	$0.6 \rightarrow 0.8$	
cAPG-F	forced flat plate	matched to cAPG-C	$0.6 \rightarrow 0.8$	
cFPG-C	curved wall	natural	$-0.5 \rightarrow -0.6$	
cFPG-F	forced flat plate	matched to cFPG-C	$-0.5 \rightarrow -0.6$	

Table 2 Computational parameters of the DNS cases. The reported wall-unit spacings correspond to the maximum values within each case group. For the low-speed cases, the domain dimensions refer to the forced flat-plate configurations.

Cases	$N_x \times N_y \times N_z$	$(L_x \times L_y \times L_z)/\delta_0$	$\Delta x^+ \times \Delta y_w^+ \times \Delta z^+$	Re_{δ_0}
iAPG	$8192 \times 320 \times 1024$	$350 \times 50 \times 20$	$9.3 \times 0.51 \times 4.3$	4220
iFPG	$8192 \times 320 \times 1024$	$350 \times 47 \times 20$	$12 \times 0.80 \times 5.7$	4220
c-cases	$9216 \times 448 \times 2048$	$350 \times 34 \times 36$	$9.9 \times 0.89 \times 4.4$	9004

3.2 Low-speed configurations

The low-speed study comprises adverse- and favourable-pressure-gradient reference cases generated by expanding and contracting upper boundaries, respectively. The APG case produces a smooth deceleration from $M \simeq 0.30$ to $M \simeq 0.24$, whereas the FPG case accelerates the flow from $M \simeq 0.30$ to $M \simeq 0.52$. In both cases, the upper boundary remains flat up to $x/\delta_0 = 75$ and subsequently follows

$$\frac{y_t}{\delta_0} = \frac{y_{t,0}}{\delta_0} + \frac{\tan\alpha}{2(350-75)}\left(\frac{x}{\delta_0} - 75\right)^2, \qquad 75 < x/\delta_0 \leq 350, \tag{34}$$

with

$$(y_{t,0}/\delta_0, \alpha) = \begin{cases} (50,\ 5^\circ), & \text{APG}, \\ (75,\ -11.24^\circ), & \text{FPG}. \end{cases} \tag{35}$$

Since these flows remain subsonic, the static pressure at the downstream boundary is relaxed towards the value of the corresponding geometrical reference solution, while the remaining variables adjust to the interior flow. For both pressure-gradient signs, the target velocity $u_e(x)$ is extracted from the inviscid region of the geometrical reference calculation. The corresponding pressure, density and temperature distributions are reconstructed from the isentropic relations, and the source terms are obtained according to §2. The forced and geometrical configurations are therefore compared at matched external-velocity evolution.

3.3 Supersonic configurations

The APG and FPG reference cases are computed using curved lower walls designed to produce prescribed boundary-layer-edge velocity distributions. The edge-velocity distributions obtained from

these simulations are then used as targets for the corresponding forced flat-plate cases. For the APG case, the target velocity is represented by

$$\frac{u_e(x)}{u_0} = 5.0346 \left[\frac{x - x_{vo}}{\delta_0}\right]^{-0.29}, \qquad \frac{x_{vo}}{\delta_0} = -183.3, \tag{36}$$

whereas the FPG target is represented by

$$\frac{u_e(x)}{u_0} = 0.629 \left[\frac{x - x_{vo}}{\delta_0}\right]^{0.1}, \qquad \frac{x_{vo}}{\delta_0} = -23.086. \tag{37}$$

The forced and curved-wall configurations are therefore compared at matched outer-flow development while differing in the presence of wall and streamline curvature. In the forced cases, $s = x$, whereas in the curved-wall cases s denotes arc length along the lower wall. The computational parameters are summarized in Table 2. Non-reflecting conditions are applied at the upper and downstream boundaries.

3.4 Statistical diagnostics

The analysis uses Reynolds averaging, $\phi = \overline{\phi} + \phi'$, and Favre averaging, $\phi = \widetilde{\phi} + \phi''$. Since the source vector is modulated by the instantaneous blending function f, its mean contribution is proportional to $\overline{f}$. For a statistically two-dimensional forced flat-plate flow, the mean continuity equation therefore reads

$$\frac{\partial(\overline{\rho}\widetilde{u})}{\partial x} + \frac{\partial(\overline{\rho}\widetilde{v})}{\partial y} = \overline{f}\, S_\rho, \tag{38}$$

and the corresponding mean streamwise momentum equation is

$$\frac{\partial(\overline{\rho}\widetilde{u}\widetilde{u})}{\partial x} + \frac{\partial(\overline{\rho}\widetilde{u}\widetilde{v})}{\partial y} = -\frac{\partial \overline{p}}{\partial x} + \frac{\partial \overline{\tau}_{xy}}{\partial y} - \frac{\partial \overline{\rho u'' u''}}{\partial x} - \frac{\partial \overline{\rho u'' v''}}{\partial y} + \overline{f}\, u_e S_\rho. \tag{39}$$

Hence, the time-averaged source distribution follows directly from the instantaneous local blending introduced in (27).

4 Low-speed validation

The low-speed validation considers the matched APG pair (iAPG-N and iAPG-F) and FPG pair (iFPG-N and iFPG-F). Within each pair, the lower-wall geometry is identical and only the mechanism used to generate the pressure gradient differs, providing a direct validation of the forcing methodology. Since both pairs exhibit comparable agreement, the discussion focuses on the APG cases, while the corresponding FPG results are reported in A. In the following, first the forcing distribution and outer-flow development are examined, followed by the boundary-layer response.

4.1 Forcing characteristics

The local action of the forcing is examined using the low-speed APG case; all remaining forced cases evaluated in this study show the same qualitative behaviour and are therefore not discussed separately. In the present implementation, the forcing mask is constructed entirely from local instantaneous flow information. This deliberately simple realization avoids global boundary-layer-edge detection and the associated inter-processor communication, while proving sufficiently robust for the attached turbulent boundary layers considered here. The present normalization is intended for attached flows; configurations approaching separation may require a vorticity-based or non-local criterion that remains well conditioned as the wall shear tends to zero. More elaborate definitions of the forcing region are possible and are independent of the source-term formulation itself.

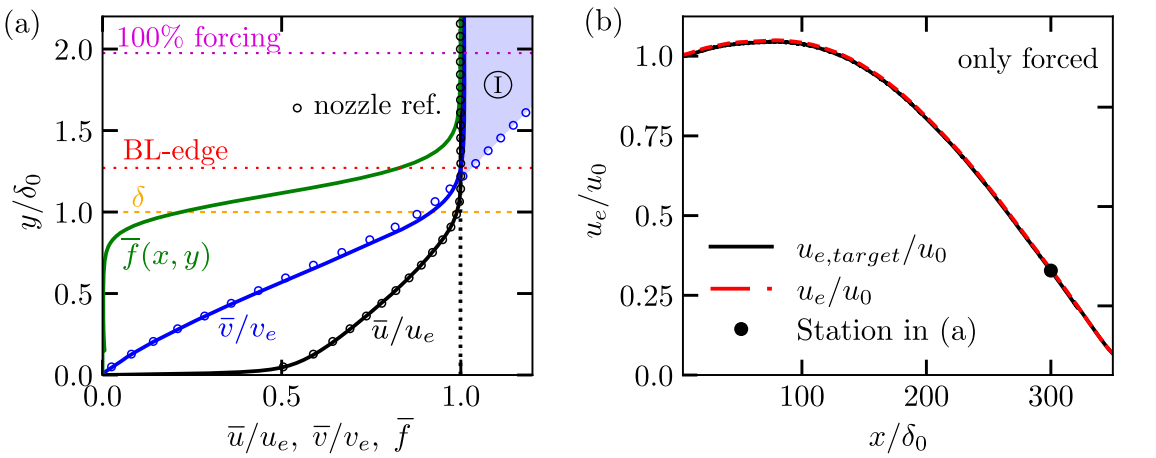


Fig. 3 Forcing characteristics for the low-speed APG case. (a) Mean streamwise and wall-normal velocity profiles and time-averaged forcing mask $\overline{f}$ at $x/\delta_0 = 300$. Open symbols denote the geometrical reference case iAPG-N. The boundary-layer thickness, boundary-layer edge and location of full forcing are indicated. Region Ⓘ highlights the different outer wall-normal mass-flux evolution of the forced and geometrical configurations. (b) Prescribed and realized boundary-layer-edge velocity distributions for the forced case iAPG-F. The marker indicates the station shown in panel (a)

At each grid point, the forcing mask is constructed from the instantaneous wall-normal gradient of the streamwise velocity, $S = \partial u/\partial y$, and normalized by its corresponding wall value $S_w = \partial u/\partial y|_w$ according to

$$\widehat{S} = \left| \frac{S}{S_w} \right|. \tag{40}$$

The forcing mask is then defined as

$$f = \frac{1}{1 + \left(\widehat{S}/S_{\text{cut}}\right)^p}, \tag{41}$$

such that $f \to 0$ where the wall-normal gradient of the streamwise velocity remains large relative to its wall value, and $f \to 1$ as $\partial u/\partial y$ approaches zero in the outer flow. Additional inner and outer guard regions enforce $f = 0$ close to the wall and $f = 1$ sufficiently far outside the boundary layer. The source contribution is therefore evaluated locally as $f\,\mathbf{S}_e(x)$ at each time step.

Figure 3 illustrates the forcing characteristics for the iAPG-F case, with panel (b) confirming the close agreement between the prescribed and realized edge-velocity evolution. In addition, analysis of the outer-flow data confirmed the expected isentropic and isenthalpic relations. Panel (a) provides a more detailed view of the local forcing at $x/\delta_0 = 300$, where the streamwise pressure gradient is strongest. The mean streamwise and wall-normal velocity profiles are shown together with the time-averaged forcing mask $\overline{f}$ and compared with the geometrical reference case iAPG-N. Since the instantaneous mask adapts to the local boundary-layer state, its time average develops a smooth wall-normal distribution reminiscent of an intermittency profile. The forcing begins to deviate from zero at approximately 75% of the boundary-layer thickness, reaches about 25% at δ and about 80% at the boundary-layer edge, and approaches its full strength only farther into the outer flow. The forcing therefore remains strongly suppressed throughout most of the boundary layer while transitioning gradually to its full outer-flow value. Within the boundary layer, the forced and geometrical solutions agree closely for both velocity components. A systematic difference appears farther outside, as indicated by region Ⓘ. In the geometrical reference case, the wall-normal velocity continues to vary across the outer flow as a consequence of the expanding nozzle geometry. In the forced configuration, this cross-stream expansion is replaced by the volumetric source terms, such that the outer wall-normal mass flux becomes nearly uniform, $\partial(\overline{\rho}\widetilde{v})/\partial y \approx 0$, while the wall-normal motion associated with the developing boundary layer is retained. It should be noted, however, that the gradual onset of the forcing in the outer part of the boundary layer may introduce small deviations once the source terms become active, most clearly visible in the v field around $y = \delta$. The extent of this influence depends on the chosen blending and can

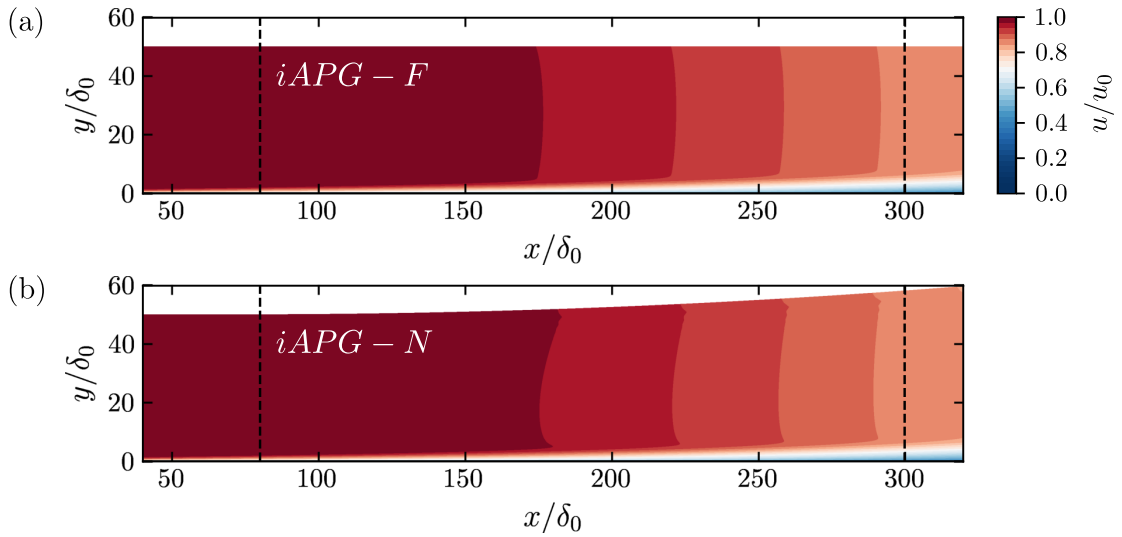


Fig. 4 Mean streamwise velocity field for the low-speed APG validation. (a) Forced configuration and (b) expanding-nozzle reference case. Vertical dashed lines indicate the stations $x/\delta_0 = 80$ and 300 used for the profile comparisons

therefore be adapted to the requirements of a particular application. While this may become relevant in laminar boundary layers or transition scenarios if disturbances in the outer part of the boundary layer play a role, no appreciable influence on the boundary-layer response is found for the turbulent cases considered here, as shown below.

4.2 Mean-flow response

For an overall view of the developed flow fields, Fig. 4 compares the mean streamwise velocity in the forced (iAPG-F) and geometrical realizations (iAPG-N). Despite the different mechanisms used to generate the pressure gradient, the streamwise development in the vicinity of the boundary layer is closely reproduced. Qualitative differences are mainly confined to the outer flow, where the streamwise-velocity isolines are noticeably more wall-normal in the forced configuration. Their remaining deviation from exact wall-normal alignment reflects the multidimensional adjustment of the Navier–Stokes solution around the imposed quasi-one-dimensional target state. The same tendency is observed in the pressure and wall-normal velocity fields (not shown). In the forced case, the pressure contours are more nearly wall-normal and the outer v field approaches the nearly uniform behaviour already indicated in Fig. 3, in contrast to the geometrically induced cross-stream development of the reference case.

A more quantitative assessment is provided in Fig. 5. Panel (a) shows the kinematic pressure-gradient parameter

$$\beta_K = \frac{\delta_K^*}{\tau_w}\frac{\mathrm{d}p_e}{\mathrm{d}x}, \tag{42}$$

where

$$\delta_K^* = \int_0^\delta \left(1 - \frac{\overline{u}}{u_e}\right)\mathrm{d}y. \tag{43}$$

The parameter β_K provides a suitable measure of pressure-gradient effects in compressible boundary layers [10]. Since it combines the imposed pressure gradient with the wall shear stress and the integral velocity-field development through δ_K^*, it constitutes a particularly stringent quantity for the present validation. The forced configuration closely follows the geometrical reference throughout the pressure-gradient region, indicating that, for the present conditions, the boundary-layer response is reproduced independently of whether the outer-flow evolution is generated geometrically or through the fictitious source terms. This is further supported by the wall-friction coefficient shown in panel (b), which likewise follows the reference closely, with only a small deviation emerging towards the end of the domain.

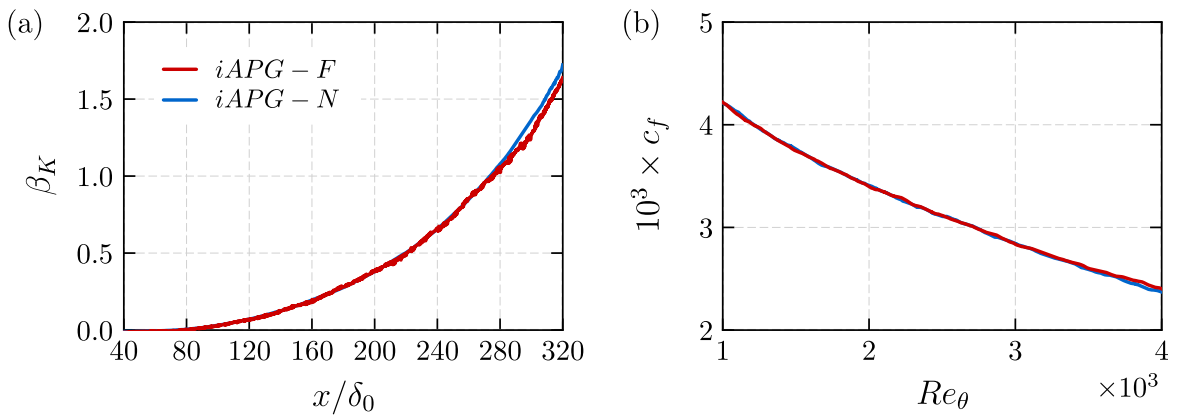


Fig. 5 Streamwise development of the pressure-gradient parameter and wall-friction coefficient for the low-speed APG validation. Red lines denote the forced flat-plate configuration and blue lines the expanding-nozzle reference case

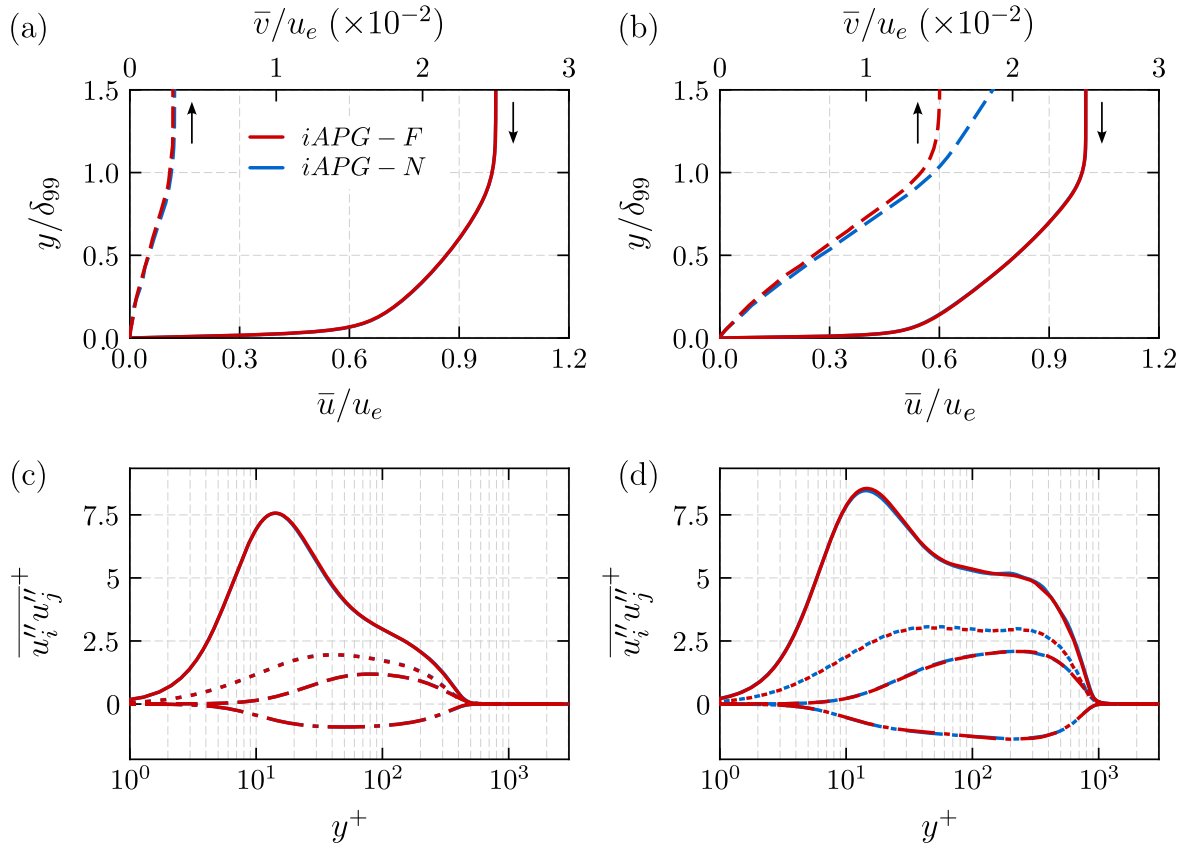


Fig. 6 Boundary-layer profiles for the low-speed APG validation. Panels (a,c) correspond to the upstream region at $x/\delta_0 = 80$, whereas panels (b,d) correspond to the APG region at $x/\delta_0 = 300$. Panels (a,b) show the mean velocity profiles and panels (c,d) the turbulent stresses. Red lines denote the forced flat-plate configuration and blue lines the expanding-nozzle reference case

Following the streamwise assessment, Fig. 6 examines the local boundary-layer structure at $x/\delta_0 = 80$ and 300, corresponding to the onset of the pressure-gradient region and a location within the strong-pressure-gradient region, respectively, see Fig. 5. Panels (a,b) show the mean streamwise and wall-normal velocity profiles in outer scaling, allowing differences between the forced and geometrical cases to be assessed more intuitively on a linear scale. The corresponding wall-unit representation yields the same level of agreement and is therefore not shown.

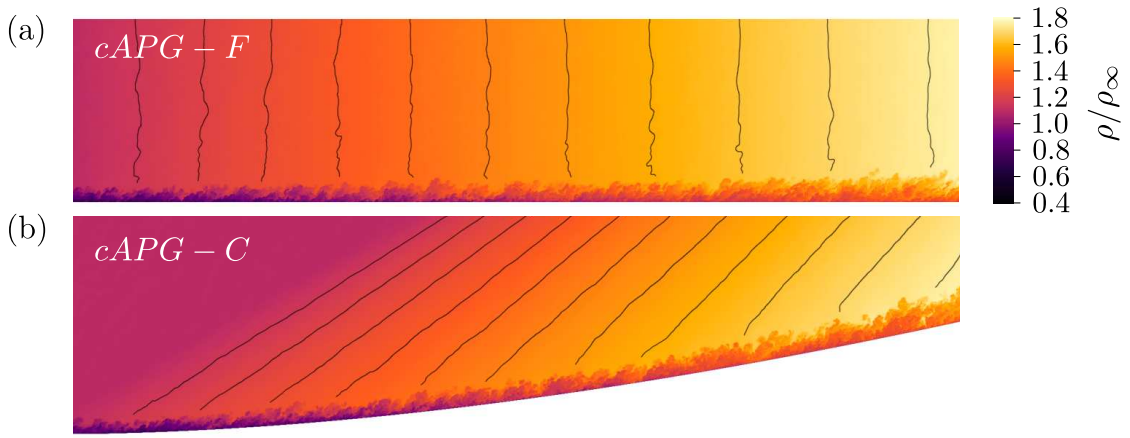


Fig. 7 Instantaneous density field for the Mach-2 APG cases. (a) Forced flat plate and (b) curved wall

Panels (c,d) show the turbulent fluctuations in wall units, using the friction velocity u_τ obtained separately from each simulation. No appreciable differences are observed between the forced and geometrical cases. This is particularly notable for the wall-normal fluctuations, which remain closely matched even at wall-normal locations extending into the outer part of the boundary layer, where small differences in the mean wall-normal velocity are already present due to the onset of the forcing. The fluctuations therefore appear largely unaffected by the small forcing-induced shift of the local mean flow.

Overall, the agreement demonstrates that the forcing reproduces both the streamwise development of the boundary layer and its local mean and turbulent structure for the subsonic cases considered. Although the present cases cover only moderate values of β_K, the pressure gradients are sufficiently strong to produce a clear response of the boundary layer and thus provide a representative test of the forcing methodology.

5 Supersonic application and comparison with curved-wall DNS

The Mach-2 configurations differ fundamentally from the low-speed validation cases, since the geometrical reference simulations employ curved lower walls and therefore contain wall- and streamline-curvature effects that are absent from the forced flat-plate configurations. The two realizations are therefore physically different, and the accuracy of the forcing method is assessed only through its ability to reproduce the prescribed boundary-layer-edge development in the forced configurations. The resulting flow fields therefore demonstrate the application of the fictitious-source formulation to supersonic pressure-gradient boundary layers and, more importantly, its ability to construct controlled flat-wall reference configurations in which the prescribed outer-flow history is retained while wall and streamline curvature are removed.

5.1 Supersonic outer-flow realization

Figures 7 and 8 provide an overview of the instantaneous density fields for the APG and FPG configurations, representative of the corresponding behaviour observed in the other flow variables. In the forced cases, panels (a), the lower wall remains flat and the pressure gradient is generated by the volumetric source terms, whereas in the geometrical reference cases, panels (b), it results from the deflection of the lower wall.

While the streamwise density variation near the boundary-layer edge is qualitatively similar within each pressure-gradient pair, pronounced differences occur in the outer flow. In the curved-wall configurations, the pressure gradient originates from the wall deflection, and the associated flow adjustment propagates downstream along characteristic directions inclined away from the surface.

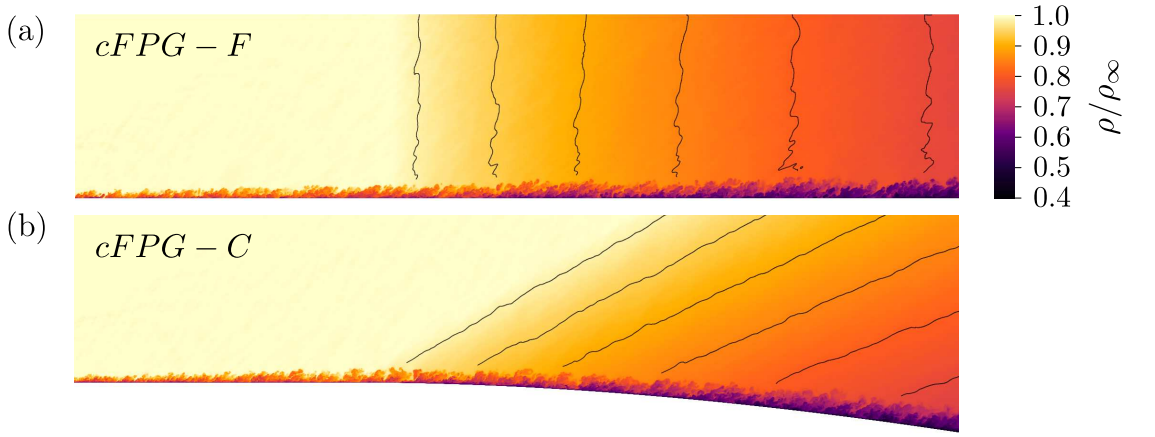


Fig. 8 Instantaneous density field for the Mach-2 FPG cases. (a) forced flat plate and (b) curved wall

In a conventional flat-wall realization, corresponding conceptually to configuration B in Fig. 2, the pressure-gradient distribution would instead have to be imposed through the outer boundary, either by an appropriate upper-wall geometry or directly through the boundary condition. The resulting disturbances propagate downstream along characteristics inclined towards the wall. A substantial streamwise distance would therefore be required for the imposed pressure information to reach the boundary-layer edge and, through superposition of incident and reflected disturbances, establish an outer pressure field with approximately wall-normal isolines [24]. Consequently, the relation between the outer-boundary prescription and the resulting pressure-gradient distribution at the boundary-layer edge remains indirect during this adjustment. Depending on Mach number and domain height, the associated adjustment region may extend over several hundred boundary-layer thicknesses and therefore introduce substantial computational overhead [24].

The fictitious-source formulation circumvents this characteristic adjustment by establishing the prescribed outer-flow evolution directly throughout the forced region. The target pressure and velocity histories can therefore be established from the onset of the pressure-gradient region, reducing the required streamwise development length and avoiding the otherwise indirect relation between the upper-boundary prescription and the resulting edge state. The nearly wall-normal density isolines in the forced cases reflect this imposed outer-flow evolution. At the same time, the formulation does not suppress the multidimensional flow response. Small disturbances generated by the boundary layer still propagate along the characteristic directions of the supersonic flow and are therefore superimposed on the prescribed quasi-one-dimensional outer-flow development. It should, however, be kept in mind that the forced far field does not represent a physical realization of the pressure-gradient flow. Rather, it provides an artificial realization of the outer flow whose purpose is to impose the desired boundary-layer-edge history without introducing the geometrical mechanisms that would normally generate it.

5.2 Outer-flow matching

In the supersonic cases, the forcing methodology is assessed by comparing the prescribed boundary-layer-edge development with that realized in the forced simulations. Figure 9 therefore provides the corresponding consistency check for the Mach-2 APG and FPG configurations.

For both pressure-gradient signs, the target distributions of u_e/u_0 are reproduced closely by the forced configurations, with only small deviations developing farther downstream. The corresponding pressure distributions likewise remain close to the isentropic target states. The forcing therefore provides accurate control of the boundary-layer-edge evolution also in the supersonic regime.

The remaining deviations are associated with the present implementation of the forcing mask rather than with the source-term formulation itself. The local blending criterion based on the wall-normal

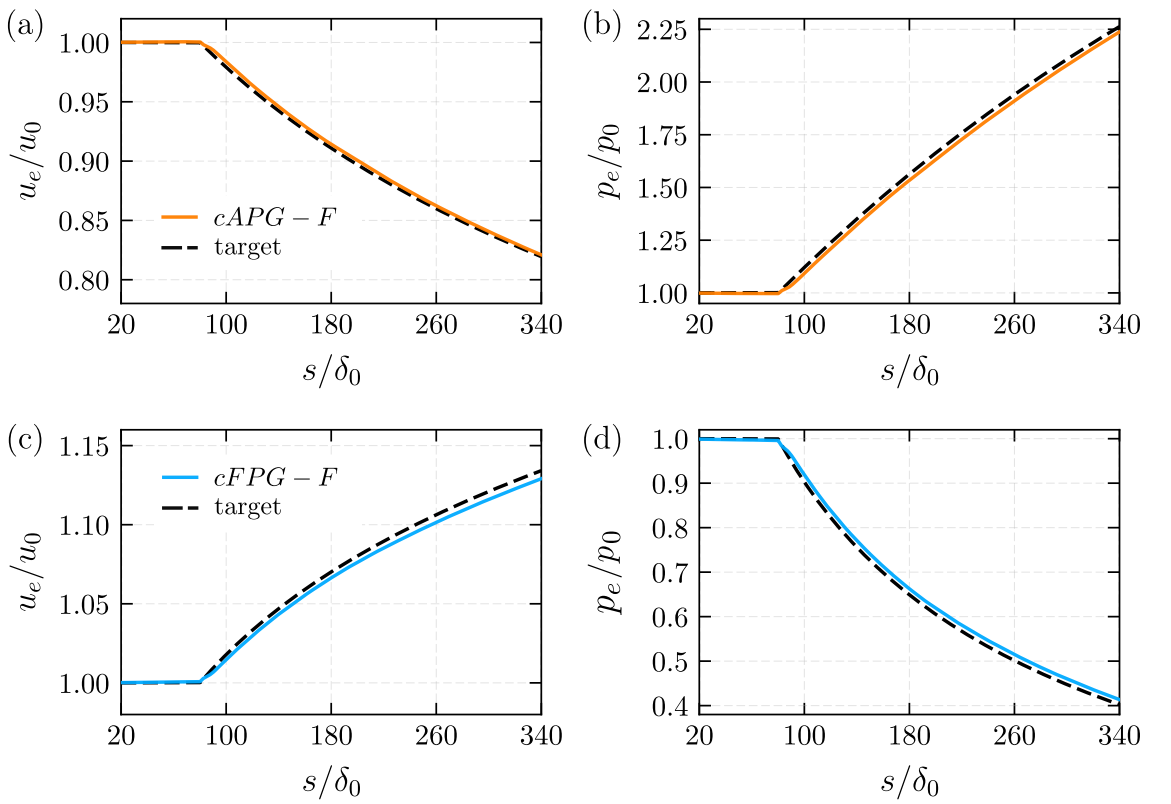


Fig. 9 Boundary-layer edge state for the Mach-2 pressure-gradient simulations. Panels (a,b) show the APG cases and panels (c,d) the FPG cases. Panels (a,c) show u_e/u_0 and panels (b,d) p_e/p_0. Line styles as in Table 1. Black dashed lines denote the reference isentropic state

velocity gradient provides a robust separation between the boundary layer and the outer flow near the boundary-layer edge. Farther outside, however, characteristic disturbances in the supersonic flow can locally prevent the blending function from approaching unity as uniformly as in the subsonic cases. More elaborate criteria, for example based on vorticity or non-local boundary-layer detection, could further reduce this sensitivity. Since the resulting deviations in u_e/u_0 and p_e/p_0 are already small for the present cases, such refinements were not pursued here. Nevertheless, monitoring the blending function has proven useful in applications of the method, since it provides a direct diagnostic of the effective forcing region and helps to identify the origin of possible deviations between the prescribed and realized outer-flow states.

5.3 Boundary-layer response

The boundary-layer response is characterized below in terms of the imposed pressure-gradient strength and the resulting integral boundary-layer development.

5.3.1 Pressure-gradient strength

As a first integral measure, Fig. 10 shows the kinematic pressure-gradient parameter β_K, providing a particularly comprehensive characterization of pressure-gradient effects as discussed for the subsonic cases. Its kinematic formulation additionally allows pressure-gradient strengths to be compared consistently across subsonic and supersonic conditions [10]. The forced and curved-wall configurations exhibit closely comparable developments and remain of the same order for both pressure-gradient signs. For the APG cases, β_K increases approximately from 0.4 to 0.6, whereas values around -0.25 are

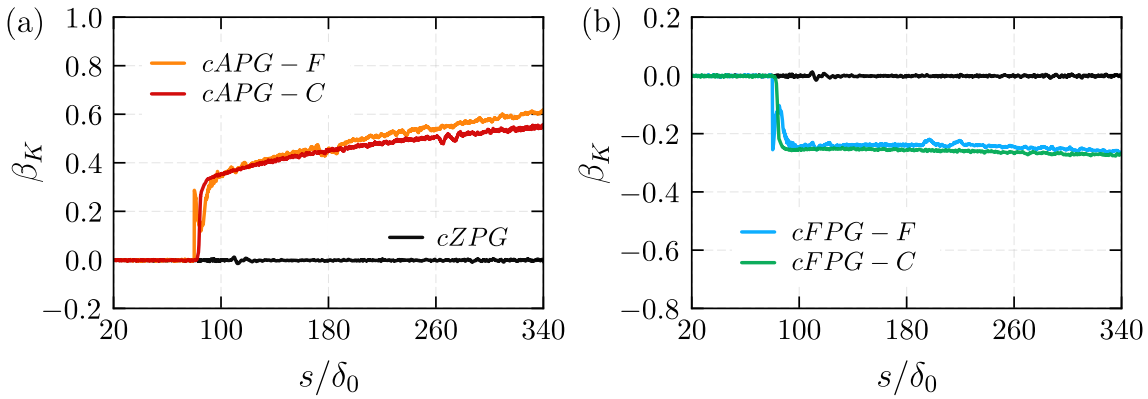


Fig. 10 Kinematic pressure-gradient parameter β_K for the Mach-2 simulations. Panel (a) shows the APG cases and panel (b) the FPG cases. Line styles as in Table 1

obtained for the FPG cases. Following this classification, the APG cases correspond to a moderate pressure-gradient strength, whereas the interpretation of the FPG cases is less direct. As discussed in [10], the progressively fuller velocity profile reduces the sensitivity of this parameter under favourable pressure gradients, such that β_K alone does not necessarily provide an equally discriminating measure of FPG strength.

Although self-similarity is not an objective of the present pressure-gradient distributions, the forcing approach is sufficiently general to accommodate approximately equilibrium outer-flow histories if desired. Such configurations may provide a useful basis for future investigations aimed at separating pressure-gradient-history and curvature effects.

5.3.2 Boundary-layer development

In the following, the boundary-layer response is compared between the forced flat-wall configurations and the corresponding curved-wall realizations. The discussion is intentionally limited to the main qualitative trends, since a detailed physical interpretation of the differences between pressure-gradient and curvature effects is beyond the scope of the present methodological study.

The spatial developments of the skin-friction coefficient c_f, the momentum thickness θ, and the boundary-layer thickness δ_{99} are shown in Fig. 11 as functions of s/δ_0. Complementary representations of c_f as a function of Re_θ, as well as the developments of the displacement thickness δ^* and Re_τ, are provided in B in Fig. 17.

Considering first the forced flat-wall configurations, the pressure-gradient effect follows the expected trend. The APG reduces c_f relative to the ZPG reference, whereas the FPG increases it. In the corresponding curved-wall configurations, this pressure-gradient response is modified by the effect of streamline curvature, which acts in the opposite direction for the present cases. For the concave APG configuration, the curvature-induced modification of the boundary layer results in a higher wall shear than in the matched flat-wall case, thereby partially compensating the reduction of c_f associated with the APG. Consequently, the skin-friction level of the curved APG case remains considerably closer to the ZPG reference than that of the forced flat-wall case. For the convex FPG configuration, the opposite behaviour is observed. Here, the FPG increases c_f, whereas the curvature-induced modification of the boundary layer leads to a lower wall shear than in the corresponding forced flat-wall case, again partially compensating the pressure-gradient effect.

Qualitatively, the momentum-thickness development exhibits a consistent behaviour. Differences in skin friction are accompanied by corresponding differences in the streamwise growth of θ, although the connection is not one-to-one because several additional terms enter the compressible momentum-integral balance. Accordingly, the curved APG case develops a larger momentum thickness than the corresponding forced case, while for the FPG pair the lower c_f of the curved-wall case is accompanied by a reduced growth of θ. This correspondence is consistent with the close connection between wall

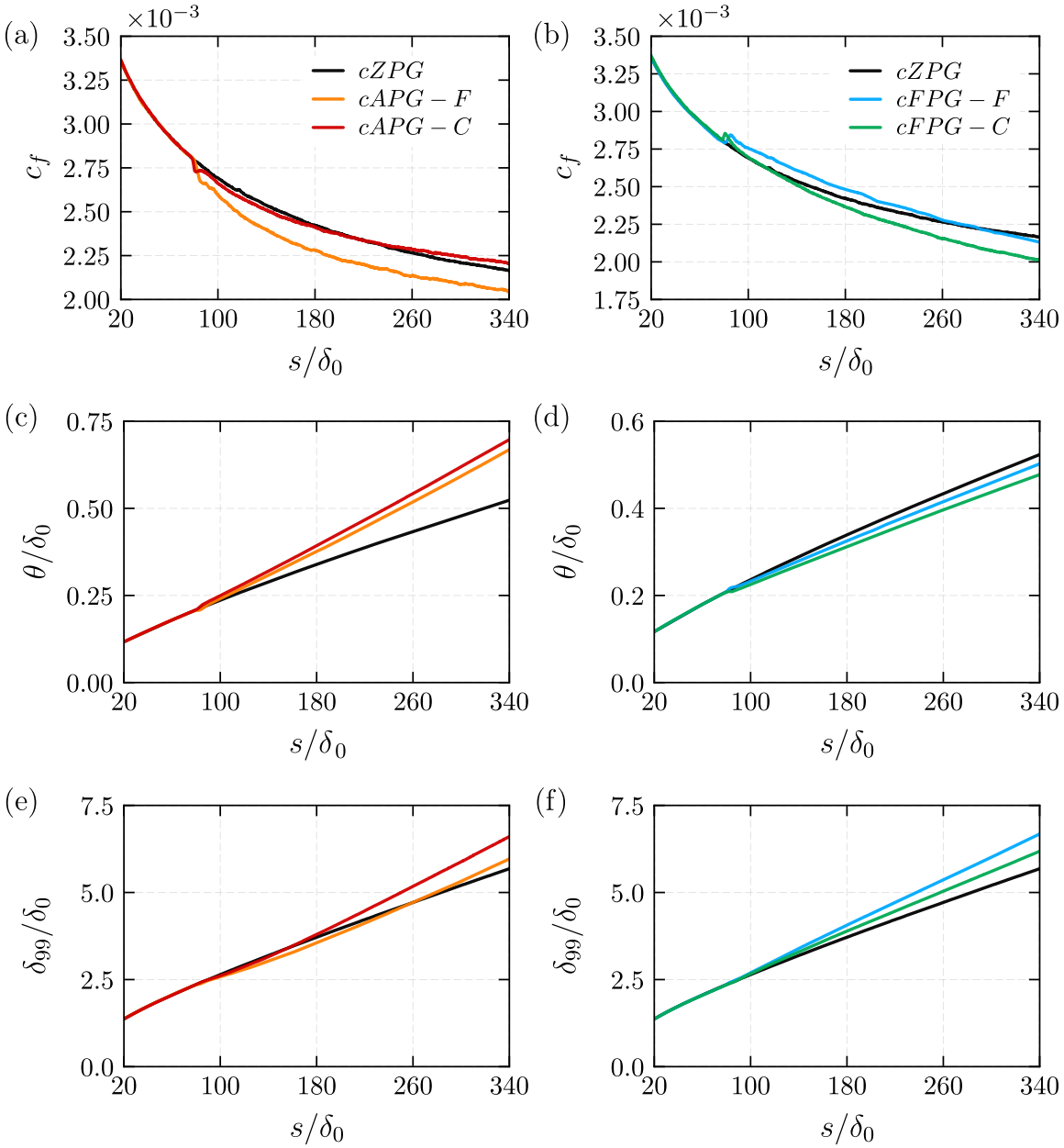


Fig. 11 Integral boundary-layer response for the Mach-2 pressure-gradient simulations. Panels (a,c,e) show the APG cases and panels (b,d,f) the FPG cases. Panels (a,b) show c_f, panels (c,d) θ/δ_0, and panels (e,f) δ_{99}/δ_0, all as functions of s/δ_0. Line styles as in Table 1

shear and momentum-thickness growth in the momentum-integral balance. This interpretation should, however, remain qualitative. As shown in the following section, the relation between c_f and the spatial development of θ is modified in the presence of curvature, since additional curvature-dependent contributions enter the momentum balance.

The interpretation of δ_{99} is additionally complicated by the compressible structure of the boundary layer. The near-wall region is necessarily subsonic, while the outer part of the Mach-2 boundary layer remains supersonic. Under adverse pressure gradients, the deceleration causes the subsonic portion to occupy an increasingly large fraction of the boundary layer, while the remaining supersonic portion becomes correspondingly thinner. Particularly when the external Mach number is reduced towards unity, this redistribution can have a substantial influence on conventional measures of boundary-layer

thickness and may lead to trends that are not immediately inferred from c_f or θ alone [24]. This behaviour is, for example, visible in the forced APG case, for which δ_{99} initially falls below the ZPG development before exceeding it again farther downstream as the external Mach number decreases.

The additional influence of wall curvature is nevertheless clearly visible. For the concave APG case, the curved-wall configuration develops a larger δ_{99} than the corresponding forced flat-wall case when plotted as a function of s/δ_0. The inward deflection associated with the concave geometry is accompanied by an increased wall-normal extent of the boundary layer, consistently with the larger momentum-thickness growth discussed above. The opposite trend is observed for the convex FPG case, for which the curved-wall configuration develops a smaller δ_{99} than the corresponding forced case. It should be kept in mind, however, that this qualitative comparison depends on the choice of streamwise coordinate and normalization used for the abscissa.

A more detailed interpretation of these interacting pressure-gradient, curvature, and compressibility effects is considerably more involved and is therefore deferred to subsequent studies focused specifically on the underlying boundary-layer physics.

5.4 Momentum-integral analysis

The von-Kármán momentum-integral relation provides a useful description of boundary-layer development by directly relating wall friction, momentum-thickness growth, and the imposed pressure gradient. While it is usually applied in its classical form derived for planar boundary layers, the present analysis explicitly retains streamline-curvature contributions through a generalized curvilinear formulation. This provides both a more complete integral description and, more importantly, a direct means of relating the curved-wall configurations to their corresponding forced flat-wall references by assessing how streamline curvature enters the momentum balance. To this end, the analysis is performed in the physical wall-fitted frame, with s denoting the arc length along the lower wall and n the local wall-normal distance. Owing to the orthogonal grid construction, the wall-normal grid lines directly provide the integration paths, while velocity and stress components are expressed in the corresponding local wall-parallel and wall-normal directions. Hereafter, u and v denote the velocity components parallel and normal to the local wall, respectively.

For the following analysis, the wall-normal variations of the mean pressure and Reynolds normal stresses are retained directly from the flow field. The streamwise viscous normal stress is neglected according to standard boundary-layer ordering, whereas the leading wall-normal shear stress is retained. Wall curvature enters explicitly through the metric and basis-rotation terms of the wall-fitted formulation, while the resulting curved-flow dynamics also modifies the boundary-layer profiles and hence the remaining contributions to the momentum balance. Two algebraically equivalent forms of the balance are considered, based respectively on the generalized and conventional momentum thicknesses. The former isolates departures from the flat-wall wall-normal stress equilibrium, whereas the latter retains the corresponding pressure and streamwise Reynolds-normal-stress contribution directly, see C for a more detailed derivation. Accordingly,

$$\begin{aligned}\tau_w = {} & \frac{\mathrm{d}}{\mathrm{d}s}\left(\rho_e u_e^2 \hat{\theta}\right) + \rho_e u_e \delta^* \frac{\mathrm{d}u_e}{\mathrm{d}s} \\ & - \frac{\mathrm{d}}{\mathrm{d}s}\left[\underbrace{\int_0^{n_e} \left(\overline{p} - p_e + \overline{\rho v'' v''}\right) \mathrm{d}n}_{I_c}\right] \\ & + \kappa_w \underbrace{\int_0^{n_e} \left(\overline{\rho}\widetilde{u}\widetilde{v} + \overline{\rho u'' v''} - \overline{\tau}_{sn}\right) \mathrm{d}n}_{I_\kappa},\end{aligned} \tag{44}$$

or, equivalently,

$$\tau_w = \frac{\mathrm{d}}{\mathrm{d}s}\left(\rho_e u_e^2 \theta\right) + \rho_e u_e \delta^* \frac{\mathrm{d}u_e}{\mathrm{d}s} - \frac{\mathrm{d}}{\mathrm{d}s}\left[\underbrace{\int_0^{n_e} \left(\overline{p} - p_e + \overline{\rho u'' u''}\right) \mathrm{d}n}_{I_s}\right] + \kappa_w I_\kappa. \tag{45}$$

Assuming a locally isentropic inviscid external flow, such that

$$\frac{1}{\rho_e}\frac{\mathrm{d}\rho_e}{\mathrm{d}s} = -M_e^2 \frac{1}{u_e}\frac{\mathrm{d}u_e}{\mathrm{d}s}, \tag{46}$$

the momentum balance may equivalently be written as

$$\frac{c_f}{2} = \frac{\mathrm{d}\hat{\theta}}{\mathrm{d}s} + \frac{2\hat{\theta} + \delta^*}{u_e}\frac{\mathrm{d}u_e}{\mathrm{d}s} - M_e^2 \frac{\hat{\theta}}{u_e}\frac{\mathrm{d}u_e}{\mathrm{d}s} - \frac{1}{\rho_e u_e^2}\frac{\mathrm{d}I_c}{\mathrm{d}s} + \frac{\kappa_w}{\rho_e u_e^2} I_\kappa, \tag{47}$$

or, equivalently,

$$\frac{c_f}{2} = \frac{\mathrm{d}\theta}{\mathrm{d}s} + \frac{2\theta + \delta^*}{u_e}\frac{\mathrm{d}u_e}{\mathrm{d}s} - M_e^2 \frac{\theta}{u_e}\frac{\mathrm{d}u_e}{\mathrm{d}s} - \frac{1}{\rho_e u_e^2}\frac{\mathrm{d}I_s}{\mathrm{d}s} + \frac{\kappa_w}{\rho_e u_e^2} I_\kappa. \tag{48}$$

Here,

$$\hat{\theta} = \theta + \frac{1}{\rho_e u_e^2}\int_0^{n_e} \overline{\rho}\left(\widetilde{v''v''} - \widetilde{u''u''}\right) \mathrm{d}n, \tag{49}$$

with

$$\theta = \int_0^{n_e} \frac{\overline{\rho}\widetilde{u}}{\rho_e u_e}\left(1 - \frac{\widetilde{u}}{u_e}\right) \mathrm{d}n, \tag{50}$$

and

$$\delta^* = \int_0^{n_e} \left(1 - \frac{\overline{\rho}\widetilde{u}}{\rho_e u_e}\right) \mathrm{d}n. \tag{51}$$

Here, equation (47) provides the basis for relating the forced and curved-wall boundary-layer responses. It decomposes the wall friction into contributions from the streamwise growth of the generalized momentum thickness, the imposed outer-flow acceleration, the corresponding Mach-number contribution, departures from wall-normal total-stress equilibrium, and the explicit curvilinear momentum flux. The latter vanishes for the forced flat-wall configurations, whereas it is finite for the curved-wall cases. It should be emphasized, however, that this decomposition does not provide a direct causal separation of the individual physical effects, since streamline curvature also modifies the boundary-layer profiles and thereby indirectly affects the remaining terms of the balance.

For the numerical evaluation, the integral quantities are smoothed using a third-order Savitzky–Golay filter with a streamwise window of $12\delta_0$. The derivatives $\mathrm{d}u_e/\mathrm{d}s$, $\mathrm{d}\theta/\mathrm{d}s$, $\mathrm{d}\hat{\theta}/\mathrm{d}s$, $\mathrm{d}I_c/\mathrm{d}s$, and $\mathrm{d}I_s/\mathrm{d}s$ are obtained by analytically differentiating the corresponding local cubic fits, such that no balance term is reconstructed from the residual. The non-differentiated factors are filtered using the same procedure before the individual contributions are formed. Robustness with respect to smoothing was verified for window widths between $8\delta_0$ and $14\delta_0$, with $12\delta_0$ adopted here. Only the interval $20 \leq s/\delta_0 \leq 340$ is reported to reduce endpoint effects.

Figure 12 shows the decomposition for the APG cases. As $\mathrm{d}u_e/\mathrm{d}s < 0$, the classical pressure-gradient contribution is negative in panel (c), whereas the Mach-number contribution is positive in panel (d) and partly compensates it. Despite the closely matched outer-flow acceleration, noticeable differences remain in both contributions because they also depend on the curvature-modified integral quantities $\widehat{\theta}$ and δ^*. The largest difference appears in the growth term $\mathrm{d}\hat{\theta}/\mathrm{d}s$, consistent with the substantially different boundary-layer development discussed above. The contribution associated with I_c remains comparatively small, while the explicit curvilinear contribution is nearly negligible for the present APG configuration.

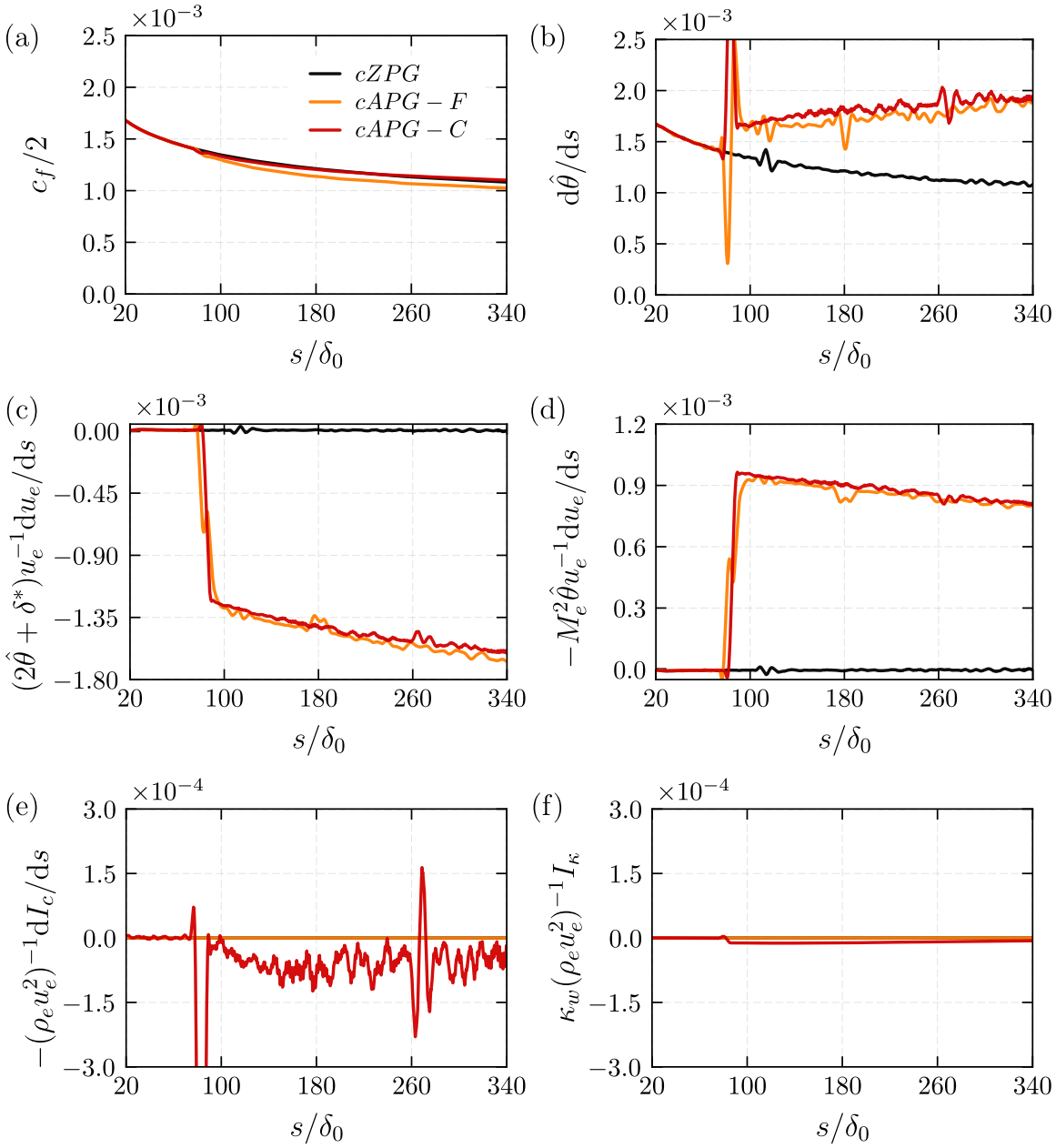


Fig. 12 Compressible mean momentum-integral balance for the Mach-2 APG simulations. Panels show (a) $c_f/2$, (b) $\mathrm{d}\hat{\theta}/\mathrm{d}s$, (c) the classical pressure-gradient contribution, (d) the Mach-number contribution, (e) the I_c contribution and (f) the I_κ contribution in (47). Line styles as in Table 1

For the FPG cases, Fig. 13, the signs of the two outer-flow-related contributions are reversed. Again, differences between the forced and curved-wall cases persist despite the closely matched $\mathrm{d}u_e/\mathrm{d}s$, because the corresponding terms also contain integral boundary-layer quantities that are modified by curvature. The reduced $\mathrm{d}\hat{\theta}/\mathrm{d}s$ of the curved-wall case accounts for a substantial part of the different momentum balance. The explicit curvilinear contribution is finite and negative, but remains small compared with the dominant terms.

Taken together, figures 12 and 13 show that the dynamical influence of curvature cannot be identified with the explicit curvilinear contribution alone. Although the imposed outer-flow acceleration is closely matched between the curved- and flat-wall configurations, curvature modifies the velocity and stress

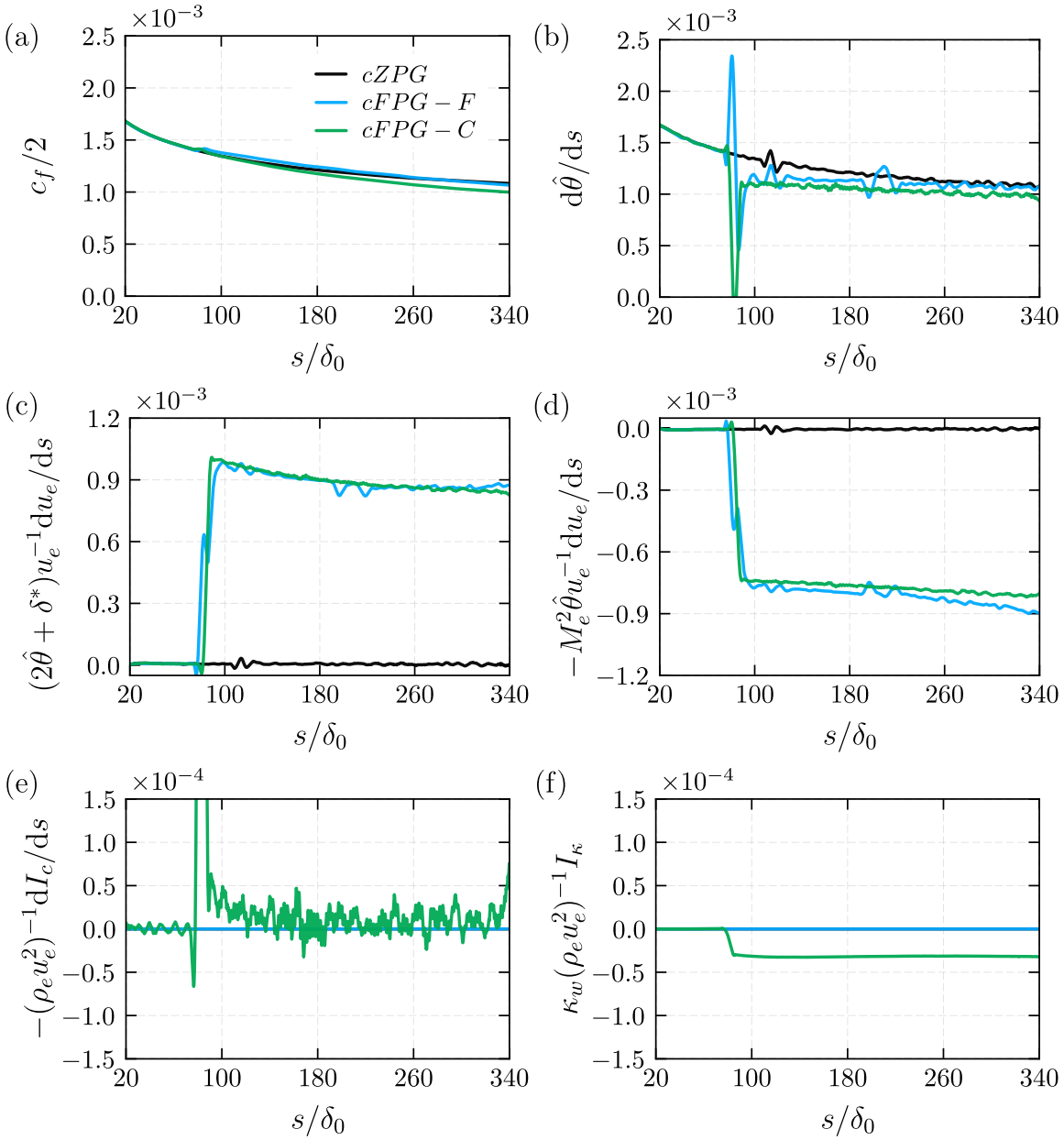


Fig. 13 Compressible mean momentum-integral balance for the Mach-2 FPG simulations. Panels show (a) $c_f/2$, (b) $\mathrm{d}\hat{\theta}/\mathrm{d}s$, (c) the classical pressure-gradient contribution, (d) the Mach-number contribution, (e) the I_c contribution and (f) the I_κ contribution in (47). Line styles as in Table 1

distributions and hence the integral boundary-layer quantities entering several terms of the momentum balance. Differences therefore appear not only in the momentum-thickness-growth term, but also in the nominal pressure-gradient and compressibility-related contributions through their dependence on $\widehat{\theta}$ and δ^*.

It is particularly noteworthy that the explicit curvature contribution $\kappa_w I_\kappa/(\rho_e u_e^2)$ is nearly negligible for the present APG case and remains small compared with the dominant terms for the FPG case. The contribution associated with I_c is likewise comparatively small, despite the appreciable differences in wall friction and integral boundary-layer development between the curved- and flat-wall configurations. Thus, for the present cases, the influence of curvature on the integral momentum balance is manifested predominantly through the curvature-induced modification of the boundary-layer state, rather than

through a large additive geometrical term. This decomposition should, however, be regarded as diagnostic rather than as a causal separation of pressure-gradient and curvature effects. A rigorous separation of the underlying mechanisms requires a more detailed analysis of the boundary-layer dynamics, for which the controlled configurations generated by the present methodology provide a suitable basis.

6 Summary and conclusions

A fictitious-source formulation has been developed for prescribing pressure-gradient histories in compressible boundary-layer DNS while retaining a flat Cartesian domain. A thermodynamically consistent quasi-one-dimensional isentropic target state is defined in the outer flow, and compatible mass, streamwise-momentum and total-energy source terms replace the streamtube expansion or contraction that would otherwise generate this evolution geometrically. Their equivalence to the source terms of a classical variable-area flow provides a direct physical interpretation of the formulation. By blending the forcing out towards the boundary layer, the desired pressure and velocity development is imposed at its edge without directly constraining the boundary-layer dynamics, including the associated wall-normal motion.

The present implementation uses a deliberately simple local criterion to distinguish the boundary layer from the forced outer flow. Since the blending adapts to the instantaneous boundary-layer state, its time average develops a smooth transition resembling an intermittency distribution. The forcing therefore becomes active gradually across the outer part of the boundary layer rather than at a sharply prescribed edge. Small deviations, most clearly in the wall-normal velocity, consequently appear already within this transition region. For the turbulent cases considered here, however, these deviations do not produce an appreciable change in the resulting mean or turbulent boundary-layer response. The simple local blending was therefore sufficient for the present purpose, while more elaborate detection criteria can be introduced independently of the source-term formulation where a sharper separation is required.

The method was validated for low-speed adverse- and favourable-pressure-gradient turbulent boundary layers against expanding- and contracting-domain reference simulations sharing the same flat lower wall. For both pressure-gradient signs, the prescribed edge-velocity development, pressure-gradient strength, wall friction, mean profiles and turbulent stresses are reproduced closely. The remaining differences are largely confined to the outer flow, where the geometrically induced cross-stream development is replaced by the imposed quasi-one-dimensional evolution.

For the supersonic cases, forced flat-wall configurations were compared with curved-wall boundary layers at closely matched boundary-layer-edge velocity histories. Despite the matched external-flow development, the different streamline geometries lead to clearly different boundary-layer responses. At the same time, the forced cases reproduce the prescribed edge velocity and pressure with only small deviations and avoid the extended adjustment associated with the propagation and superposition of disturbances along Mach characteristics in geometrical or outer-boundary realizations.

A generalized momentum-integral analysis provides additional insight into how these differences enter the streamwise momentum balance. As expected, the influence of curvature is not confined to the explicit curvilinear term, but is also reflected indirectly through the curvature-modified boundary-layer profiles and the associated momentum-thickness-growth, pressure-gradient and compressibility-related contributions. The decomposition therefore provides an integral perspective on the coupled response rather than a unique separation of the underlying physical mechanisms.

A more detailed analysis of these interacting effects requires a dedicated investigation of the underlying boundary-layer dynamics. The principal outcome of the present methodology is therefore not a surrogate for curved-wall flow, but a means of reproducing its prescribed pressure-gradient history independently of the geometry that generated it. This provides a controlled framework for separating pressure-gradient, curvature and compressibility effects in high-speed turbulent boundary layers.

Acknowledgements This work was supported by the Air Force Office of Scientific Research under Grant No. FA8655-23-1-7016. The computational resources were provided by Regular and Extreme Access Projects on the EuroHPC Joint Undertaking Infrastructure resource Leonardo at CINECA.

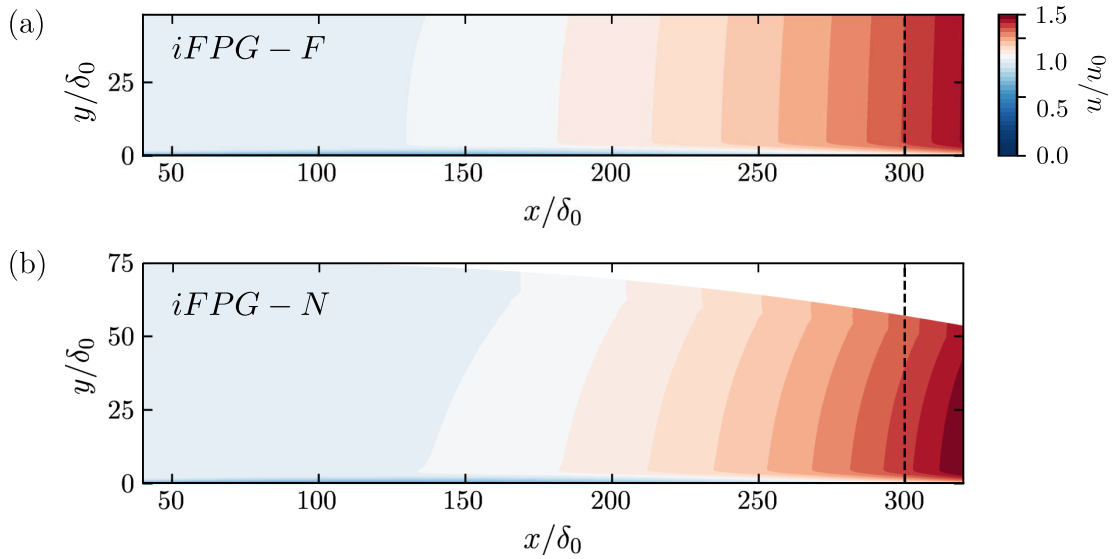


Fig. 14 Mean streamwise velocity field for the low-speed FPG validation. (a) Forced flat-plate configuration and (b) converging-nozzle reference case. The same contour levels are used in both panels. Vertical dashed lines indicate the stations at $x/\delta_0 = 300$ used for the profile comparisons

CRediT authorship contribution statement Alessandro Ceci: Writing – review & editing, Writing – original draft, Software, Methodology, Investigation, Formal analysis; Christoph Wenzel: Writing – review & editing, Writing – original draft, Methodology, Investigation, Formal analysis; Sergio Pirozzoli: Writing – review & editing, Writing – original draft, Supervision, Methodology, Formal analysis, Conceptualization.

Data availability The data sets generated during and/or analysed during the current study are available from the corresponding author on reasonable request.

Declarations

Conflict of interest The authors report no conflict of interest.

Appendix A Low-speed FPG validation

The complementary low-speed FPG validation is shown in Figs. 14–16. The geometrical reference employs a converging upper boundary, whereas the corresponding forced configuration retains a Cartesian domain. Figure 14 compares the resulting mean streamwise velocity fields. In the converging-nozzle reference, the external flow is accelerated by the geometrical contraction, whereas the same acceleration is generated volumetrically in the forced configuration. As in the APG case discussed in the main text, the forced outer flow remains more nearly one-dimensional, while the streamwise development in the vicinity of the boundary layer is closely reproduced.

The corresponding pressure-gradient development is shown in Fig. 15(a). The acceleration produced by the converging nozzle leads to the expected decrease of the pressure-gradient parameter, which is closely reproduced by the forced configuration. The resulting wall-friction coefficient in Fig. 15(b) likewise shows very good agreement between the two realizations.

The agreement is further confirmed by the wall-normal profiles in Fig. 16 at $x/\delta_0 = 300$, where the favourable pressure gradient is fully established. Both the mean velocity components and the turbulent stresses of the forced configuration remain closely matched to the converging-nozzle reference.

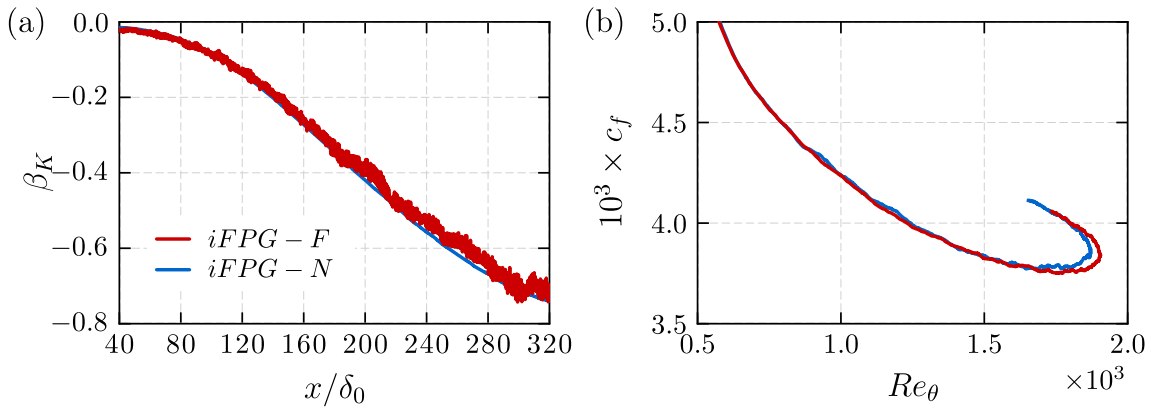


Fig. 15 Low-speed FPG validation. (a) Pressure-gradient parameter and (b) wall-friction coefficient. Red lines denote the forced configuration and blue lines the converging-nozzle reference case

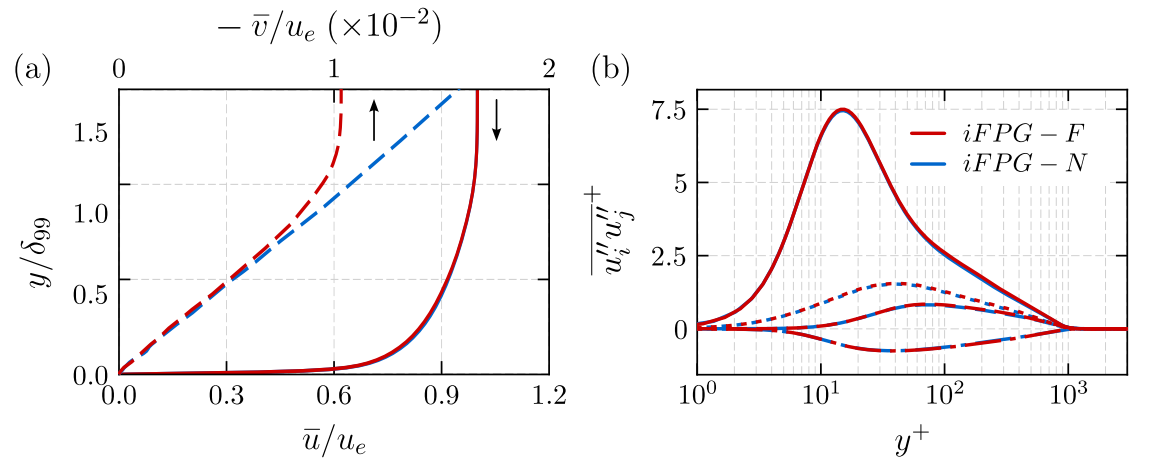


Fig. 16 Wall-normal profiles for the low-speed FPG validation at $x/\delta_0 = 300$. Panel (a) shows the mean streamwise and wall-normal velocities and panel (b) the turbulent stresses. Red lines denote the forced configuration and blue lines the converging-nozzle reference case

Appendix B Additional boundary-layer quantities for the Mach-2 cases

Additional measures of the integral boundary-layer response are shown in Fig. 17. Panels (a,b) compare the skin friction at matched Re_θ, removing the direct influence of the different streamwise Reynolds-number development from the comparison. The forced and curved-wall configurations remain clearly separated, showing that the differences in wall friction cannot be attributed solely to a shift in the streamwise boundary-layer development.

The displacement thicknesses in panels (c,d) show corresponding differences in the integral mass deficit, while panels (e,f) compare the friction Reynolds number. Together with the quantities presented in Fig. 11, these results further demonstrate that the matched outer pressure-gradient histories do not lead to identical boundary-layer evolution when wall and streamline curvature are present.

Appendix C Complete derivation of the mean momentum-integral balance in wall-fitted coordinates

We derive here the mean momentum-integral balance used in the analysis. A physical wall-fitted frame (s, n) is introduced, where s denotes arc length along the lower wall and n is the wall-normal distance,

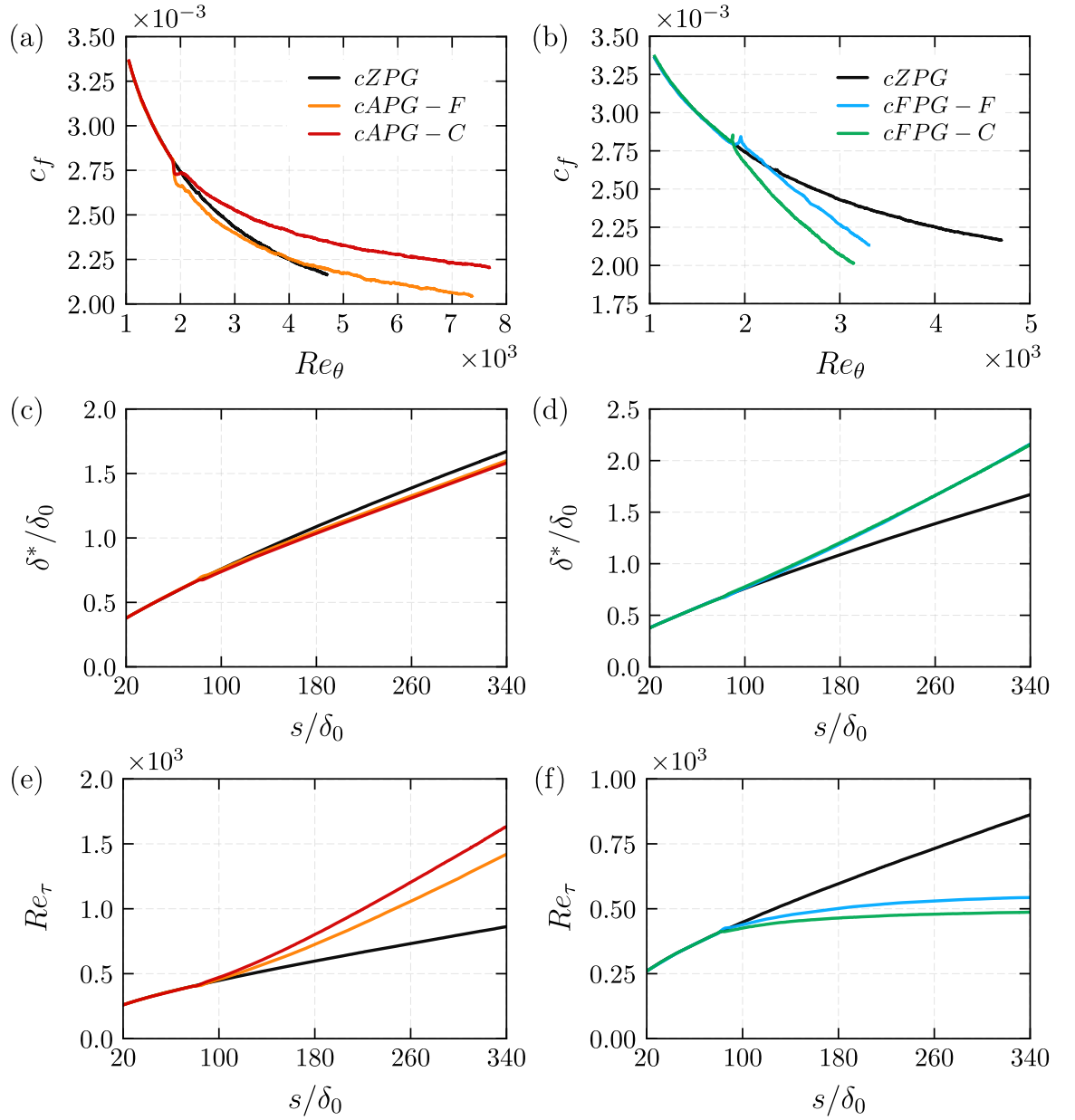


Fig. 17 Additional boundary-layer quantities for the Mach-2 pressure-gradient simulations. Panels (a,c,e) show the APG cases and panels (b,d,f) the FPG cases. Panels (a,b) show c_f as a function of Re_θ, panels (c,d) δ^*/δ_0 as a function of s/δ_0, and panels (e,f) Re_τ as a function of s/δ_0. Line styles as in Table 1

directed into the fluid. The corresponding unit tangent and normal vectors satisfy

$$\frac{\mathrm{d}\boldsymbol{t}}{\mathrm{d}s} = \kappa_w \boldsymbol{n}, \qquad \frac{\mathrm{d}\boldsymbol{n}}{\mathrm{d}s} = -\kappa_w \boldsymbol{t}, \tag{C1}$$

where κ_w is the signed wall curvature. Points in the wall-normal neighbourhood are represented as

$$\boldsymbol{x}(s,n) = \boldsymbol{x}_w(s) + n\boldsymbol{n}(s), \tag{C2}$$

for which the wall-parallel metric factor is

$$\mathcal{G}(s,n) = 1 - \kappa_w(s) n. \tag{C3}$$

Hereafter, u and v denote the velocity components parallel and normal to the local wall, respectively.

For a statistically stationary and two-dimensional flow, the Favre-averaged continuity equation, after multiplication by the metric factor, reads

$$\frac{\partial}{\partial s}\left(\overline{\rho}\widetilde{u}\right)+\frac{\partial}{\partial n}\left(\mathcal{G}\overline{\rho}\widetilde{v}\right)=0. \tag{C4}$$

The corresponding wall-parallel momentum equation is

$$\begin{aligned}0=&\frac{\partial}{\partial s}\left(\overline{\rho}\widetilde{u}^{\,2}\right)+\frac{\partial\overline{p}}{\partial s}+\frac{\partial}{\partial s}\left(\overline{\rho}\widetilde{u''u''}\right)-\frac{\partial\overline{\tau}_{ss}}{\partial s}\\&+\frac{\partial}{\partial n}\left(\mathcal{G}\overline{\rho}\widetilde{u}\widetilde{v}\right)+\frac{\partial}{\partial n}\left(\mathcal{G}\overline{\rho}\widetilde{u''v''}\right)-\frac{\partial}{\partial n}\left(\mathcal{G}\overline{\tau}_{sn}\right)\\&-\kappa_w\overline{\rho}\widetilde{u}\widetilde{v}-\kappa_w\overline{\rho}\widetilde{u''v''}+\kappa_w\overline{\tau}_{sn}.\end{aligned} \tag{C5}$$

The terms proportional to κ_w arise from the rotation of the wall-fitted basis and vanish identically for a flat wall.

The wall-normal momentum equation is

$$\begin{aligned}0=&\frac{\partial}{\partial s}\left(\overline{\rho}\widetilde{u}\widetilde{v}\right)+\frac{\partial}{\partial s}\left(\overline{\rho}\widetilde{u''v''}\right)-\frac{\partial\overline{\tau}_{sn}}{\partial s}\\&+\frac{\partial}{\partial n}\left(\mathcal{G}\overline{\rho}\widetilde{v}^{\,2}\right)+\frac{\partial}{\partial n}\left(\mathcal{G}\overline{p}\right)+\frac{\partial}{\partial n}\left(\mathcal{G}\overline{\rho}\widetilde{v''v''}\right)-\frac{\partial}{\partial n}\left(\mathcal{G}\overline{\tau}_{nn}\right)\\&+\kappa_w\overline{\rho}\widetilde{u}^{\,2}+\kappa_w\overline{p}+\kappa_w\overline{\rho}\widetilde{u''u''}-\kappa_w\overline{\tau}_{ss}.\end{aligned} \tag{C6}$$

Under the usual boundary-layer ordering, the leading wall-normal balance becomes

$$\mathcal{G}\frac{\partial}{\partial n}\left(\overline{p}+\overline{\rho}\widetilde{v''v''}\right)+\kappa_w\left[\overline{\rho}\widetilde{u}^{\,2}+\overline{\rho}\widetilde{u''u''}-\overline{\rho}\widetilde{v''v''}\right]\simeq 0. \tag{C7}$$

Hence, for a flat wall, the total wall-normal stress is uniform across the boundary layer, whereas finite curvature introduces a cross-layer variation.

To obtain the integral wall-parallel balance, (C4) is multiplied by the edge velocity $u_e(s)$ and (C5) is subtracted. After adding and subtracting the edge pressure gradient, one obtains

$$\begin{aligned}0=&\frac{\partial}{\partial s}\left[\overline{\rho}\widetilde{u}\left(u_e-\widetilde{u}\right)\right]-\overline{\rho}\widetilde{u}\frac{\mathrm{d}u_e}{\mathrm{d}s}\\&-\frac{\partial}{\partial s}\left(\overline{p}-p_e\right)-\frac{\mathrm{d}p_e}{\mathrm{d}s}-\frac{\partial}{\partial s}\left(\overline{\rho}\widetilde{u''u''}\right)+\frac{\partial\overline{\tau}_{ss}}{\partial s}\\&+\frac{\partial}{\partial n}\left[\mathcal{G}\overline{\rho}\widetilde{v}\left(u_e-\widetilde{u}\right)\right]-\frac{\partial}{\partial n}\left(\mathcal{G}\overline{\rho}\widetilde{u''v''}\right)+\frac{\partial}{\partial n}\left(\mathcal{G}\overline{\tau}_{sn}\right)\\&+\kappa_w\left[\overline{\rho}\widetilde{u}\widetilde{v}+\overline{\rho}\widetilde{u''v''}-\overline{\tau}_{sn}\right].\end{aligned} \tag{C8}$$

Equation (C8) is integrated between the wall and a boundary-layer edge $n_e(s)$. At the edge we assume $\widetilde{u}=u_e$, $\overline{p}=p_e$, with negligible turbulent and viscous shear stresses, whereas at the wall $\widetilde{u}=\widetilde{v}=0$ and $\overline{\tau}_{sn}=\tau_w$. Since the streamwise defect quantities vanish at $n=n_e$, the terms associated with differentiation of the upper integration limit also vanish. The resulting balance is

$$\begin{aligned}\tau_w=&\frac{\mathrm{d}}{\mathrm{d}s}\left[\int_0^{n_e}\overline{\rho}\widetilde{u}\left(u_e-\widetilde{u}\right)\mathrm{d}n\right]\\&-\frac{\mathrm{d}}{\mathrm{d}s}\left[\int_0^{n_e}\left(\overline{p}-p_e+\overline{\rho}\widetilde{u''u''}\right)\mathrm{d}n\right]+\frac{\mathrm{d}}{\mathrm{d}s}\left[\int_0^{n_e}\overline{\tau}_{ss}\mathrm{d}n\right]\\&-\frac{\mathrm{d}u_e}{\mathrm{d}s}\int_0^{n_e}\overline{\rho}\widetilde{u}\mathrm{d}n-n_e\frac{\mathrm{d}p_e}{\mathrm{d}s}\\&+\kappa_w\int_0^{n_e}\left[\overline{\rho}\widetilde{u}\widetilde{v}+\overline{\rho}\widetilde{u''v''}-\overline{\tau}_{sn}\right]\mathrm{d}n.\end{aligned} \tag{C9}$$

Introducing the compressible momentum and displacement thicknesses,

$$\theta = \int_0^{n_e} \frac{\overline{\rho}\widetilde{u}}{\rho_e u_e}\left(1 - \frac{\widetilde{u}}{u_e}\right) \mathrm{d}n, \qquad \delta^* = \int_0^{n_e} \left(1 - \frac{\overline{\rho}\widetilde{u}}{\rho_e u_e}\right) \mathrm{d}n, \tag{C10}$$

gives

$$\int_0^{n_e} \overline{\rho}\widetilde{u}\,(u_e - \widetilde{u})\,\mathrm{d}n = \rho_e u_e^2 \theta, \tag{C11}$$

and

$$\int_0^{n_e} \overline{\rho}\widetilde{u}\mathrm{d}n = \rho_e u_e\,(n_e - \delta^*)\,. \tag{C12}$$

The terms involving the edge velocity and pressure gradients may therefore be rearranged as

$$\begin{aligned} -\frac{\mathrm{d}u_e}{\mathrm{d}s}\int_0^{n_e} \overline{\rho}\widetilde{u}\mathrm{d}n - n_e\frac{\mathrm{d}p_e}{\mathrm{d}s} &= \rho_e u_e \delta^* \frac{\mathrm{d}u_e}{\mathrm{d}s} \\ &\quad - n_e\left(\rho_e u_e \frac{\mathrm{d}u_e}{\mathrm{d}s} + \frac{\mathrm{d}p_e}{\mathrm{d}s}\right). \end{aligned} \tag{C13}$$

At boundary-layer order, the inviscid tangential momentum balance at the edge gives

$$\frac{\mathrm{d}p_e}{\mathrm{d}s} = -\rho_e u_e \frac{\mathrm{d}u_e}{\mathrm{d}s}, \tag{C14}$$

so that the term proportional to n_e in (C13) vanishes, leaving only the displacement-thickness contribution.

The streamwise viscous normal stress is higher order in the boundary-layer expansion. In particular,

$$\frac{\partial_s \tau_{ss}}{\partial_n \tau_{sn}} = O\left[\left(\frac{\delta}{L}\right)^2\right], \tag{C15}$$

and its contribution is therefore neglected, whereas τ_{sn} is retained as the leading molecular stress. The momentum-integral balance then becomes

$$\tau_w = \frac{\mathrm{d}}{\mathrm{d}s}\left(\rho_e u_e^2 \theta\right) + \rho_e u_e \delta^* \frac{\mathrm{d}u_e}{\mathrm{d}s} - \frac{\mathrm{d}I_s}{\mathrm{d}s} + \kappa_w I_\kappa, \tag{C16}$$

where

$$I_s = \int_0^{n_e} \left(\overline{p} - p_e + \overline{\rho}\widetilde{u''u''}\right) \mathrm{d}n, \tag{C17}$$

and

$$I_\kappa = \int_0^{n_e} \left[\overline{\rho}\widetilde{u}\widetilde{v} + \overline{\rho}\widetilde{u''v''} - \overline{\tau}_{sn}\right] \mathrm{d}n. \tag{C18}$$

The latter represents the explicit curvilinear momentum-flux contribution and is multiplied by the signed wall curvature.

An equivalent representation is obtained by defining the generalized momentum thickness

$$\hat{\theta} = \theta + \frac{1}{\rho_e u_e^2}\int_0^{n_e} \overline{\rho}\left(\widetilde{v''v''} - \widetilde{u''u''}\right) \mathrm{d}n, \tag{C19}$$

and the wall-normal total-stress defect

$$I_c = \int_0^{n_e} \left(\overline{p} - p_e + \overline{\rho}\widetilde{v''v''}\right) \mathrm{d}n. \tag{C20}$$

By construction,

$$\rho_e u_e^2 \hat{\theta} - I_c = \rho_e u_e^2 \theta - I_s, \tag{C21}$$

and hence (C16) is equivalently written as

$$\tau_w = \frac{\mathrm{d}}{\mathrm{d}s}\left(\rho_e u_e^2 \hat{\theta}\right) + \rho_e u_e \delta^* \frac{\mathrm{d}u_e}{\mathrm{d}s} - \frac{\mathrm{d}I_c}{\mathrm{d}s} + \kappa_w I_\kappa. \tag{C22}$$

The two forms are therefore algebraically identical. The quantity I_c measures departures from wall-normal total-stress equilibrium, whereas $\kappa_w I_\kappa$ accounts for the explicit geometrical contribution associated with the rotation of the wall-fitted frame.

Finally, dividing (C22) by $\rho_e u_e^2$ gives

$$\frac{c_f}{2} = \frac{\mathrm{d}\hat{\theta}}{\mathrm{d}s} + \frac{\hat{\theta}}{\rho_e}\frac{\mathrm{d}\rho_e}{\mathrm{d}s} + \frac{2\hat{\theta}+\delta^*}{u_e}\frac{\mathrm{d}u_e}{\mathrm{d}s} - \frac{1}{\rho_e u_e^2}\frac{\mathrm{d}I_c}{\mathrm{d}s} + \frac{\kappa_w}{\rho_e u_e^2} I_\kappa. \tag{C23}$$

No thermodynamic assumption concerning the edge state has been invoked in this form. For a locally isentropic inviscid external flow,

$$\frac{1}{\rho_e}\frac{\mathrm{d}\rho_e}{\mathrm{d}s} = -M_e^2 \frac{1}{u_e}\frac{\mathrm{d}u_e}{\mathrm{d}s}, \tag{C24}$$

and the balance reduces to

$$\frac{c_f}{2} = \frac{\mathrm{d}\hat{\theta}}{\mathrm{d}s} + \frac{2\hat{\theta}+\delta^*}{u_e}\frac{\mathrm{d}u_e}{\mathrm{d}s} - M_e^2 \frac{\hat{\theta}}{u_e}\frac{\mathrm{d}u_e}{\mathrm{d}s} - \frac{1}{\rho_e u_e^2}\frac{\mathrm{d}I_c}{\mathrm{d}s} + \frac{\kappa_w}{\rho_e u_e^2} I_\kappa. \tag{C25}$$

The equivalent expression in terms of θ and I_s follows directly from (C21). For a flat wall, $\kappa_w = 0$, while wall-normal total-stress equilibrium additionally implies $I_c = 0$. In the ZPG limit with constant edge conditions, the usual relation $c_f/2 = \mathrm{d}\hat{\theta}/\mathrm{d}s$ is recovered [5].

References

1. Adams, N.A.: Direct simulation of the turbulent boundary layer along a compression ramp at $M = 3$ and $Re_\theta = 1685$. Journal of Fluid Mechanics **420**, 47–83 (2000). https://doi.org/10.1017/S0022112000001257
2. Appelbaum, J., Kloker, M., Wenzel, C.: A systematic DNS approach to isolate wall-curvature effects in spatially developing boundary layers. Theoretical and Computational Fluid Dynamics **39**, 10 (2025). https://doi.org/10.1007/s00162-024-00729-7
3. Bernardini, M., Modesti, D., Salvadore, F., Pirozzoli, S.: STREAmS: A high-fidelity accelerated solver for direct numerical simulation of compressible turbulent flows. Computer Physics Communications **263**, 107,906 (2021). https://doi.org/10.1016/j.cpc.2021.107906
4. Bradshaw, P.: The effect of streamline curvature on turbulent flow. AGARDograph **169** (1973)
5. Ceci, A., Palumbo, A., Larsson, J., Pirozzoli, S.: Numerical tripping of high-speed turbulent boundary layers. Theoret. Comput. Fluid Dyn. **36**(6), 865–886 (2022). https://doi.org/10.1007/s00162-022-00623-0
6. Donovan, J.F., Spina, E.F., Smits, A.J.: The structure of a supersonic turbulent boundary layer subjected to concave surface curvature. Journal of Fluid Mechanics **259**, 1–24 (1994). https://doi.org/10.1017/S0022112094000017
7. Dörr, P.: Numerical investigation of crossflow transition control using plasma actuators. Verlag Dr. Hut (2018). PhD thesis
8. Fang, J., Yao, Y., Zheltovodov, A.A., Li, Z., Lu, L.: Direct numerical simulation of supersonic turbulent flows around a tandem expansion-compression corner. Physics of Fluids **27**, 125,104 (2015). https://doi.org/10.1063/1.4936576
9. Gatski, T.B., Bonnet, J.P.: Compressibility, turbulence and high speed flow, 2 edn. Academic Press (2013). URL https://www.sciencedirect.com/book/9780123970275/compressibility-turbulence-and-high-speed-flow
10. Gibis, T., Wenzel, C., Kloker, M., Rist, U.: Self-similar compressible turbulent boundary layers with pressure gradients. Part 2. self-similarity analysis of the outer layer. Journal of Fluid Mechanics **880**, 284–325 (2019). https://doi.org/10.1017/jfm.2019.672

11. Na, Y., Moin, P.: Direct numerical simulation of a separated turbulent boundary layer. Journal of Fluid Mechanics **374**, 379–405 (1998). https://doi.org/10.1017/S0022112098009987
12. Pargal, S., Wu, H., Yuan, J., Moreau, S.: Adverse-pressure-gradient turbulent boundary layer on convex wall. Physics of Fluids **34**, 035,107 (2022). https://doi.org/10.1063/5.0083919
13. Perry, A.E., Marusic, I., Jones, M.B.: On the streamwise evolution of turbulent boundary layers in arbitrary pressure gradients. Journal of Fluid Mechanics **461**, 61–91 (2002). https://doi.org/10.1017/S002211200200825X
14. Pirozzoli, S.: Generalized conservative approximations of split convective derivative operators. J. Comput. Phys. **229**, 7180–7190 (2010). https://doi.org/10.1016/j.jcp.2010.06.006
15. Pirozzoli, S., Bernardini, M., Grasso, F.: Direct numerical simulation of transonic shock/boundary layer interaction under conditions of incipient separation. J. Fluid Mech. **657**, 361–393 (2010). https://doi.org/10.1017/S0022112010001710
16. Salvadore, F., Soldati, G., Ceci, A., Rossi, G., Memmolo, A., Della Posta, G., Modesti, D., Sathyanarayana, S., Bernardini, M., Pirozzoli, S.: Streams-2.1: Supersonic turbulent accelerated navier-stokes solver version 2.1. Computer Physics Communications **314**, 109,652 (2025). https://doi.org/10.1016/j.cpc.2025.109652
17. Smits, A.J., Dussauge, J.P.: Turbulent Shear Layers in Supersonic Flow. Springer (2006). https://doi.org/10.1007/b137383
18. Sun, M., Hu, Z., Sandham, N.D.: Recovery of a supersonic turbulent boundary layer after an expansion corner. Physics of Fluids **29**, 076,103 (2017). https://doi.org/10.1063/1.4995293
19. Sun, M., Sandham, N.D., Hu, Z.W.: Turbulence structures and statistics of a supersonic turbulent boundary layer subjected to concave surface curvature. Journal of Fluid Mechanics **865**, 60–99 (2019). https://doi.org/10.1017/jfm.2019.19
20. Vinuesa, R., Hosseini, S.M., Hanifi, A., Henningson, D.S., Schlatter, P.: Pressure-gradient turbulent boundary layers developing around a wing section. Flow, Turbulence and Combustion **99**, 613–641 (2017). https://doi.org/10.1007/s10494-017-9840-z
21. Wang, Q., Wang, Z., Zhao, Y.: An experimental investigation of the supersonic turbulent boundary layer subjected to concave curvature. Physics of Fluids **28**, 096,104 (2016). https://doi.org/10.1063/1.4962563
22. Wang, Q., Wang, Z., Zhao, Y.: On the impact of adverse pressure gradient on the supersonic turbulent boundary layer. Physics of Fluids **28**, 116,101 (2016). https://doi.org/10.1063/1.4968527
23. Wassermann, P., Kloker, M.: Transition mechanisms in a three-dimensional boundary-layer flow with pressure-gradient changeover. Journal of Fluid Mechanics **530**, 265–293 (2005). https://doi.org/10.1017/S0022112005003708
24. Wenzel, C., Gibis, T., Kloker, M., Rist, U.: Self-similar compressible turbulent boundary layers with pressure gradients. part 1. direct numerical simulation and assessment of Morkovin's hypothesis. Journal of Fluid Mechanics **880**, 239–283 (2019). https://doi.org/10.1017/jfm.2019.670
25. Wray, A.: Minimal storage time advancement schemes for spectral methods. NASA Ames Research Center, California, Report No. MS **202** (1990)
26. Wu, M., Martin, M.P.: Direct numerical simulation of supersonic turbulent boundary layer over a compression ramp. AIAA Journal **45**, 879–889 (2007). https://doi.org/10.2514/1.27021
27. You, J., Buchta, D.A., Zaki, T.A.: Concave-wall turbulent boundary layers without and with free-stream turbulence. Journal of Fluid Mechanics **915**, A4 (2021). https://doi.org/10.1017/jfm.2021.12